AGU ADVANCING EARTH AND SPACE SCIENCES

JGR Solid Earth

RESEARCH ARTICLE
10.1029/2026JB034505

The Impact of Double Subduction on Plate Velocity and Euler Pole Shifts: Insights From Spherical Subduction Models

Zonglin Guo[1], **Adam F. Holt**[1], **and Derya Gürer**[2]

[1]Rosentiel School of Marine, Atmospheric, and Earth Science, University of Miami, Miami, FL, USA, [2]Institute of Earth Sciences, Heidelberg University, Heidelberg, Germany

Key Points:

- Same-dip double subduction strongly impacts plate velocities and corresponding Euler poles in 3-D spherical models
- Plate velocity changes arise from increased slab pull and reduced plate area contributing to basal-drag resistance
- Plate and trench geometry control relative velocity differences and Euler pole shifts more strongly than rheological parameters

Supporting Information:

Supporting Information may be found in the online version of this article.

Correspondence to:

Z. Guo,
guo.zonglin@miami.edu

Citation:

Guo, Z., Holt, A. F., & Gürer, D. (2026). The impact of double subduction on plate velocity and Euler pole shifts: Insights from spherical subduction models. *Journal of Geophysical Research: Solid Earth*, *131*, e2026JB034505. https://doi.org/10.1029/2026JB034505

Received 7 APR 2026
Accepted 27 AUG 2026

Author Contributions:

Conceptualization: Zonglin Guo, Adam F. Holt
Formal analysis: Zonglin Guo, Adam F. Holt, Derya Gürer
Funding acquisition: Adam F. Holt
Investigation: Zonglin Guo
Methodology: Zonglin Guo, Adam F. Holt
Project administration: Adam F. Holt
Resources: Zonglin Guo, Adam F. Holt
Software: Zonglin Guo
Supervision: Adam F. Holt
Validation: Zonglin Guo, Adam F. Holt, Derya Gürer
Visualization: Zonglin Guo

Abstract Same-dip double subduction (SDDS), in which two parallel slabs dip in the same direction, has been linked to accelerated plate motion in both modern and ancient convergent systems, such as the Late Cretaceous Africa–Eurasia system. Yet a systematic framework for quantifying how SDDS alters plate kinematics in a large-scale spherical geometry is lacking. Here, we use 3-D spherical geodynamic models to investigate plate velocity changes and corresponding Euler pole shifts caused by the insertion of a second (rear) subduction zone. Across a wide range of rheological and geometric parameters, SDDS consistently increases the velocity of the subducting plate, especially behind the rear trench, redirects subducting-plate motion toward the rear slab, and produces pronounced Euler pole shifts of up to 33° (~3,600 km). We complement the numerical models with a torque-balance analysis, which shows that these dramatic plate velocity changes arise from two primary effects: (a) additional slab pull exerted by the added slab and (b) a reduction in the effective subducting-plate area contributing to basal-drag resistance. This plate-area reduction is the dominant contributor to Euler pole displacement, with enhanced slab pull providing a secondary but reinforcing effect. We characterize the impact of an extensive set of model parameters: plate and mantle rheology primarily modify velocity magnitudes, while geometric factors that modify plate and trench geometry govern the relative velocity differences (e.g., Euler pole shifts) between the single- and double-subduction geometries. Our spherical subduction modeling provides a generalized geodynamic framework for interpreting plate-motion reorganizations associated with intra-oceanic subduction initiation and termination.

Plain Language Summary Earth's tectonic plates move as their cold, dense edges sink into Earth's interior at subduction zones, providing a "pull" that drags plates across the surface. In some regions, two parallel subduction zones sink in the same direction, creating a "same-dip double subduction" system. Such systems have been linked to times in Earth's history when plates moved at particularly high speeds, for example, during the convergence of Africa and Eurasia. However, we do not yet fully understand how, and to what extent, a second subduction zone influences the speed and direction of plate motion. We used 3-D spherical computer models of Earth's mantle to investigate how plate velocities change when a second rear subduction zone is inserted. We find that double subduction consistently speeds up plates and changes their direction of motion. Our analysis shows that these changes are driven by two factors: (a) the added rear slab exerts slab pull directly on the plate segment behind the rear trench and (b) the added subduction zone reduces the portion of the subducting plate that resists motion, making the plate easier to move. These modeling results show that the formation of new subduction zones can drive major, large-scale changes in tectonic plate motion.

1. Introduction

Subduction plays a central role in the evolution of the solid Earth, and many subduction systems involve interacting slabs whose coupled dynamics influence magmatism, deformation, and mantle flow (e.g., Forsyth & Uyeda, 1975; Stern, 2002). Double subduction zones, where two nearby slabs coexist and interact, are widespread on Earth, including in the Mediterranean (e.g., Király et al., 2018; Vignaroli et al., 2008), Taiwan (e.g., Lallemand et al., 2001; Lin & Kuo, 2016), the Molucca Sea (e.g., Di Leo et al., 2014; Q. Zhang et al., 2017), the Caribbean Sea (e.g., van Benthem et al., 2013; K. Zhang et al., 2024), and on either side of the Philippine Sea Plate (e.g., Faccenna et al., 2018; Hall, 2002). Geological reconstructions further indicate that double subduction systems were also common in the past, including in the Neo-Tethys, which upon closure led to the Africa-Eurasia

Writing – original draft: Zonglin Guo
Writing – review & editing: Zonglin Guo, Adam F. Holt, Derya Gürer

(Gürer et al., 2022; Stampfli & Borel, 2002) and India–Eurasia collisions (Besse & Courtillot, 1988; Jagoutz et al., 2015), as well as in the North Pacific (Domeier et al., 2017; Hu et al., 2022; Konstantinovskaia, 2001).

Double subduction zones can be classified by the relative geometry of the two slabs: inward-dipping (toward each other), outward-dipping (away from each other), opposite-dipping (passing in opposite directions), and same-dip (subducting in parallel). Among these, same-dip double subduction (SDDS) zones appear to be uniquely associated with anomalously high plate velocities and large-scale plate kinematic reorganizations. For example, SDDS and the associated onset of plate velocity changes are well documented within the Neo-Tethyan system. In the central part of the Neo-Tethyan SDDS system, the convergence of the Indian and Eurasian continents reached anomalously high speeds of >14 cm/yr prior to the 50–40 Ma collision (Besse & Courtillot, 1988; Cande & Stegman, 2011). In the western Neo-Tethys, the African plate accelerated from ∼2–3 to ∼4.5–8 cm/yr, between 108 and 92 Ma, with significant rotation of plate motion direction (Gürer et al., 2022; van Hinsbergen et al., 2020) following the onset of SDDS. Conversely, the termination of an intra-oceanic subduction zone, and hence the transition from SDDS to a single subduction zone, can also impact plate velocities. For example, in the Northwest Pacific, the ∼50 Ma cessation of subduction at the intra-oceanic Kronotsky subduction zone aligns with a major change in plate motion direction (Domeier et al., 2017; Hu et al., 2022; Konstantinovskaia, 2001; Vaes et al., 2019).

Previous numerical modeling studies of SDDS have investigated the influence of an additional subduction zone on plate velocities. Both 2-D and 3-D numerical models demonstrate that SDDS enhances plate velocities relative to equivalent single subduction models, because a portion of the slab pull force from the frontal slab is transmitted to the rear subducting plate (e.g., Holt et al., 2017; Jagoutz et al., 2015; Pusok & Stegman, 2019). However, most existing numerical models do not account for a potentially finite lateral extent of the intra-plate trench, in which the rear trench occupies only part of the entire subducting-plate width. This geometry is critical for understanding plate-velocity changes induced by a transition from single to double subduction, as the previous analogue experiments show that along-strike asymmetry in subduction can generate non-uniform velocities and produce plate rotation (Wang et al., 2024). In natural systems, intra-oceanic trenches commonly display significant geometric complexity and have limited lateral extents, which can result in non-uniform along-strike plate velocities (e.g., Gürer et al., 2022). Such plate velocity variations lead to plate rotations, and hence changes in the locations of the Euler poles that describe plate motion on a sphere. These changes cannot be captured within either 2-D (e.g., Faccenna et al., 2018; Mishin et al., 2008) or 3-D models that set trench widths equal to the entire subducting plate (e.g., Holt et al., 2017; Pusok & Stegman, 2019). Therefore, 3-D models incorporating finite intra-plate trench extents are needed to rigorously quantify how the addition of a second same-dip intra-oceanic subduction zone affects plate velocities.

Global kinematic models provide a framework for reconstructing plate motions through time by deriving self-consistent plate motions based on Euler pole rotations on a sphere (e.g., Seton et al., 2012). However, these reconstructions are limited by the fragmented geological record of oceanic domains and often simplify regions of high geometric complexity, such as double subduction zones, where the physical drivers of motion changes remain poorly understood. This highlights the need for geodynamic models that can quantify plate motion changes through Euler pole shifts, including those associated with double subduction (e.g., DeMets et al., 2010; Gürer et al., 2022; van Hinsbergen et al., 2020), and provide a physical basis for interpreting plate tectonic reconstructions. Moreover, in some of the most striking cases of SDDS, such as the Cretaceous Neo-Tethys and present-day Philippine–Pacific systems, the rear subducting plate is large, with dimensions greater than 5,000 km. For such large plates, with widths greater than ∼2,400 km, Earth's sphericity exerts a significant influence on plate velocities (Chaillat et al., 2024; Chen et al., 2022). These considerations further motivate the need to investigate SDDS dynamics at a larger scale than within regional domains and within a spherical domain. Several previous studies have utilized larger-scale numerical models to examine various aspects of subduction dynamics, including the impact of slab remnants on subduction dynamics (Chen et al., 2024), the influence of plate sphericity on free subduction (Chaillat et al., 2024; Chen et al., 2022), and subduction-induced mantle pressure and flow fields (Holt, 2022). Other studies have employed large-scale modeling frameworks to investigate specific subduction systems, such as the India–Eurasia collision (Li et al., 2024) and the plate velocity change recorded by the Hawaii–Emperor chain (e.g., Hu et al., 2022; J. Zhang & Hu, 2025). However, to our knowledge, no study has employed spherical subduction models to systematically evaluate how geodynamic parameters and material properties govern plate motions within large-scale double subduction systems.

We therefore develop and analyze spherical double subduction models, evaluating the impact of a range of key physical parameters previously shown to influence subduction dynamics: slab/mantle viscosity contrast (Billen & Hirth, 2007; Stegman et al., 2010), interface strength (Behr & Becker, 2018; Čížková & Bina, 2013), mantle rheology (Cui et al., 2024; Holt & Becker, 2016; Zhong et al., 1998), subducting plate length (Holt & Becker, 2016; Xue et al., 2020), plate width (Schellart et al., 2007; Stegman et al., 2006), trench length and separation (Faccenna et al., 2018; Jagoutz et al., 2015), and obliquity (Balázs et al., 2021; Wada et al., 2015). The selection of these parameters is inspired by the geometric complexities observed in real-world tectonic systems, such as the highly irregular, jagged patterns for the intraoceanic trench of Neo-Tethys (e.g., Gürer et al., 2016; Maffione & van Hinsbergen, 2018), which we approximate using a simplified set of geometric variables. All such parameters have absolute values that are either uncertain (e.g., slab strength) or exhibit broad ranges on Earth (e.g., obliquity and plate width/length). We therefore examine a large suite of models that systematically vary these parameters to capture the associated range of impacts on plate motion.

To isolate the impact of double subduction on plate velocities, we compare pairs of equivalent single and double subduction models within 3-D spherical domains. Our models therefore quantify the plate-motion differences between end-member configurations rather than simulating the initiation or termination of the second subduction zone itself. By holding properties constant within such model pairs, aside from the addition of a second subduction zone, we systematically evaluate how double subduction influences plate motion across a diverse range of rheological and geometric variables. We evaluate double subduction-induced changes in plate velocity magnitude, direction, and the best-fit Euler pole position, since the latter provides an integrated descriptor of plate motion on a sphere. The results indicate that absolute plate speeds are particularly sensitive to rheological parameters, whereas differences in plate motion between single and double subduction models are more sensitive to geometric variables (e.g., plate size and trench separation). To isolate the main mechanisms within our numerical models, we also apply a torque-balance analysis to reproduce the first-order numerical model behavior. We find that plate velocity changes induced by SDDS are driven by two primary mechanisms. The first is the additional slab pull exerted by the added rear slab, a process well studied previously. Second, a reduction in the effective subducting-plate area, that is, the area contributing to basal-drag resistance, also increases plate velocity. This reduction requires faster plate motion to generate an equivalent resisting basal-drag torque, and therefore represents a previously unrecognized but critical factor in producing these plate-kinematic changes. This result remains consistent across all tested variables, providing a mechanical framework for the dramatic plate velocity changes reconstructed in natural systems such as the Neo-Tethys.

2. Method

2.1. Model Strategy

We construct 3-D spherical subduction models with whole-mantle domains using the ASPECT finite-element code, version 2.6.0-pre (Bangerth et al., 2023; Heister et al., 2017; Kronbichler et al., 2012). The input geometries, including the plate and slab structures, are generated using the Geodynamic World Builder (Fraters, 2023; Fraters et al., 2019). Our goal is to characterize plate-velocity differences between prescribed single and double subduction end-member configurations, rather than to simulate subduction initiation or the subsequent self-consistent evolution of the slabs. The double subduction geometry represents a stage in which a second intra-oceanic rear trench and its associated slab have already become established. We therefore adopt pseudo-instantaneous models, run for only 10 kyr, short enough that plate and slab geometries undergo minimal evolution from their imposed configurations. Hence the initiation of intra-oceanic subduction, due for example to the deformation and weakening of the downgoing oceanic plate, is not simulated here. We adopt this pseudo-instantaneous approach in order to directly compare plate velocities, and hence the underlying force balance, between the single and double subduction cases without the need to correct for variable trench, plate, and slab geometries. Our approach therefore relies on the implicit assumption that plate motion varies relatively smoothly between these two states.

The models neglect thermal diffusion and do not solve the energy equation. Instead, the governing system reduces to conservation of mass and momentum for incompressible creeping flow:

$$\nabla \cdot \mathbf{u} = 0 \tag{1}$$

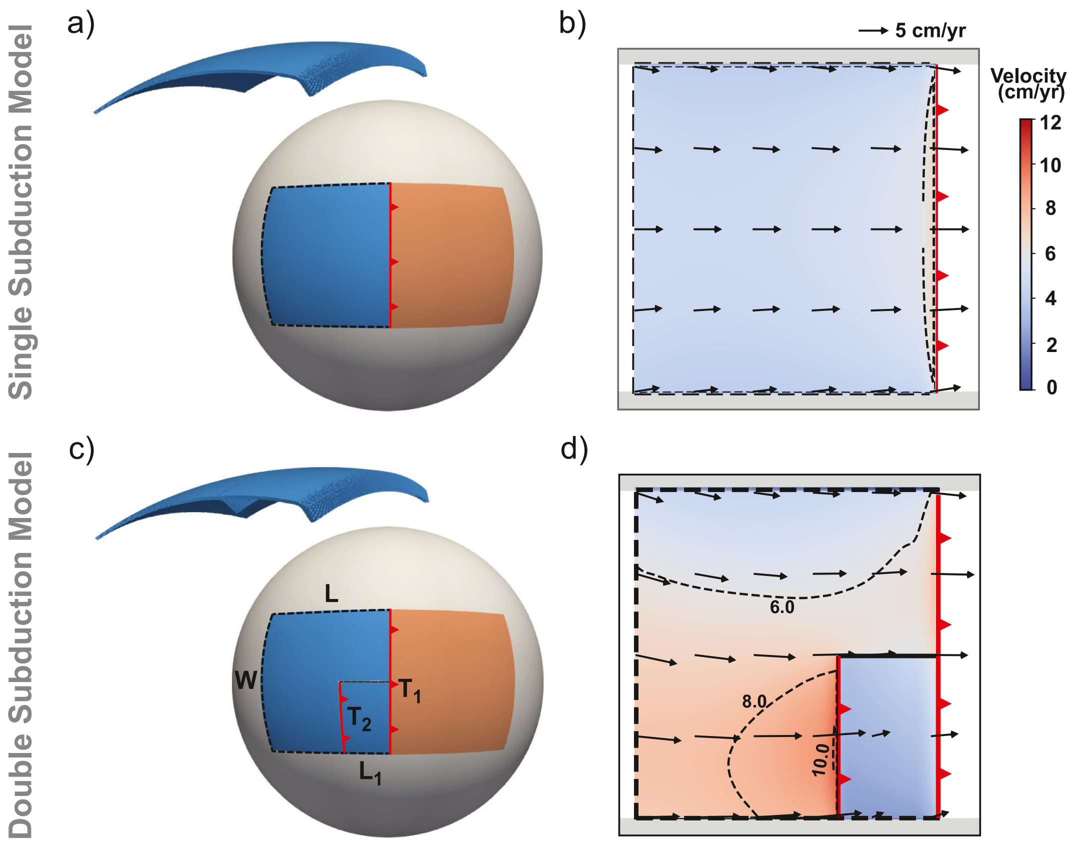

Figure 1. Plate and slab geometries of (a) the reference single subduction model and (c) the reference double subduction model, with (b) and (d) showing their respective plate-velocity distributions at 20 km depth. Red lines represent trench locations, subducting plates are outlined by black dashed lines, and the thick black solid line in (c) represents the weak zone. L denotes plate length, W denotes plate width and is equal to the frontal trench length T_1, T_2 denotes rear-trench length, and L_1 denotes trench separation. Side plates (not shown) are separated from the subducting plate by 50-km-wide weak zones. Velocity contours are shown by thin dashed black lines.

$$\nabla P + \nabla \cdot 2\eta\dot{\varepsilon}(\mathbf{u}) + \rho\mathbf{g} = 0 \quad (2)$$

where $\mathbf{u}$ is velocity, P is pressure, η is viscosity as a function of composition, $\dot{\varepsilon}$ is the strain-rate tensor derived from the velocity field, and ρ is the composition-dependent density. Material properties are assigned through compositional fields rather than temperature: density and rheological parameters are composition-dependent, with isoviscous crustal and lithospheric layers and a strain-rate-dependent mantle. Six compositional fields are included: the crust and lithosphere of the overriding plate, crust and lithospheric mantle of the subducting plate, lithosphere of the side plate, and the weak zones. The weak zone material is used for two weak zones: vertical decoupling zones situated between the subducting and adjacent side plates, and an intra-plate connector that links the front and rear trenches in the double subduction models. This connector acts as a simplified mechanical decoupling zone, rather than a self-consistent representation of a lithospheric shear zone. Both weak zones have equivalent properties. All boundaries are mechanically free slip. We use this simplified boundary condition to focus on plate-scale-velocity changes, while noting that free-surface and elastic effects, which are not included here, may affect shallow stresses, trench motion, and near-surface deformation (e.g., Crameri & Tackley, 2016; Patočka et al., 2019).

2.2. Reference Model Setup

In our reference single slab model (Figure 1a), both the subducting and overriding plates are square, with side lengths of 45° (≈5,000 km). To reduce trench-parallel plate shortening, two half-width side plates are included, separated from the subducting plate by 50-km-wide weak zones (Yamato et al., 2009). The slab has a radius of curvature of 280 km at the surface, transitioning into a straight segment that dips at 60° between depths of 140 and 450 km (the maximum depth). Phase transitions are not included for simplicity, so the imposed slab-tip depth controls the initial slab-pull contribution without additional buoyancy effects associated with mantle phase transitions. Sensitivity to the prescribed slab-tip depth is assessed separately below. All plates are 100 km thick, including a 15-km-thick weak crustal layer at the top of both the subducting and overriding plates, and along the upper slab surface to 120 km depth (Figure S1 in Supporting Information S1). This crustal layer makes up the plate boundary shear zone, which facilitates decoupling and relative convergence between the two plates. In the reference double slab model (Figure 1c), an intra-oceanic slab is inserted with the same geometry as the frontal slab, and decoupled from the subducting plate by a trench-perpendicular, 25 km-wide weak zone cutting through the lithospheric plates and extending between the two trenches. The second trench is located one-third of the plate length away (1,700 km) from the frontal trench, with a trench length of 2,500 km (half the frontal trench length).

Both the lithosphere and crust have constant densities of 3,375 kg/m^3, which is 75 kg/m^3 denser than the sub-lithospheric mantle. The lithospheric and crustal layers are isoviscous, and in the underlying sub-lithospheric mantle, we employ a composite rheology combining Newtonian and power-law behavior (Zhong et al., 1998), in order to mimic the first-order effects of diffusion and dislocation creep, respectively. Lithospheric plates are set to be 500 times more viscous (10^{23} Pa s) than the reference mantle viscosity (2×10^{20} Pa s) and the crustal layer has a viscosity of 10^{20} Pa s. For deep plate-interface temperatures of 500–600°C and a reference strain rate of 10^{-12} s^{-1} (e.g., simple shear across a 3-km-wide zone driven by a ~10 cm/yr convergence rate), this crustal viscosity lies between experimental estimates for strong meta-basalts and weaker metasediments and serpentinites (Behr & Becker, 2018; Tokle et al., 2023).

Power-law flow in the mantle is included due to its large effect on plate and trench motions (Holt & Becker, 2016; Čížková & Bina, 2013). The Newtonian viscosity component of the mantle, η_N, is set to 4×10^{20} Pa s. The power-law component, η_P, is calculated by reducing η_N within high strain rate regions following:

$$\eta_P = \eta_N \left(\dot{\epsilon}/\dot{\epsilon}_T\right)^{\frac{1-n}{n}} \tag{3}$$

where $\dot{\epsilon}$ is the square root of the second invariant of the strain rate tensor and n is the power-law exponent (=3.5), a value representative of olivine dislocation creep (e.g., Hirth & Kohlstedt, 2003). $\dot{\epsilon}_T$ is the transition strain rate, where the Newtonian and power-law viscosities are equal, and hence controls the proportion of the domain within the power-law regime. A lower value shifts a greater proportion of the deforming sub-lithospheric mantle into the power-law domain and therefore represents a weaker mantle endmember. This remains a simplified parameterization: the isoviscous plates impose a discrete viscosity contrast at the plate base, rather than the smooth lithosphere–asthenosphere transition of a thermal lithosphere with temperature-dependent viscosity. We assume a transition strain rate of 5×10^{-15} s^{-1} (e.g., Holt & Becker, 2016), at which the power-law viscosity matches the Newtonian mantle viscosity, that is, $\eta_P = \eta_N = 4 \times 10^{20}$ Pa s. The effective model viscosity is then calculated as:

$$\eta_{\text{eff}} = \left(\frac{1}{\eta_N} + \frac{1}{\eta_P}\right)^{-1} \tag{4}$$

which produces the reference viscosity of $\eta_{\text{eff}} = 2 \times 10^{20}$ Pa s. Below the 660-km discontinuity, viscosity increases by a factor of 50 relative to the reference upper mantle value (Moresi & Gurnis, 1996). The lateral and trench-perpendicular weak zones both have a constant viscosity equal to the upper mantle reference value (2×10^{20} Pa s) and the density of lithospheric plates (3,375 kg/m^3).

2.3. Model Variables

We construct and analyze pairs of models with a range of rheological and geometrical parameters. Three rheological parameters are examined: lithosphere/mantle viscosity contrast η_L/η_M, crust/mantle viscosity contrast η_C/η_M, and power-law transition strain rate $\dot{\epsilon}$. We also varied four geometric parameters: plate width W, plate length L, trench separation L_1/L, and trench length ratio T_2/T_1. These geometric variables are illustrated in Figure 1c, and the values are detailed below.

Relative to the reference crust/mantle viscosity contrast $(\eta_C/\eta_M = 0.5)$, we test a higher value of 2 ($\eta_C = 4 \times 10^{20}$ Pa s) and a lower value of 0.1 ($\eta_C = 2 \times 10^{19}$ Pa s), to approximate stronger meta-basalts and weaker metasediments and serpentinites, respectively (e.g., Behr & Becker, 2018). For the lithosphere/mantle viscosity contrast (η_L/η_M), we also examine low and high ratios of 100 ($\eta_L = 2 \times 10^{22}$ Pa s) and 2,000 ($\eta_L = 4 \times 10^{23}$ Pa s), corresponding to weak and strong end members of the range inferred from, for example, geoid constraints, slab shapes and trench motions (Billen & Hirth, 2007; Funiciello et al., 2008; Ribe, 2010; Schellart, 2009). Following Holt and Becker (2016), we also test low and high values of the transition strain rate, of 10^{-15} s^{-1} and 10^{-14} s^{-1}. Varying the transition strain rate, which is broadly analogous to varying the power-law pre-factor within temperature-dependent flow laws, serves to bracket uncertainty in mantle strength within our compositional models. A lower transition strain rate shifts a larger fraction of the deforming sub-lithospheric mantle into the power-law regime and therefore represents a weaker mantle end member, particularly in high-strain-rate regions around the subducting slab.

Regarding the parameters that govern plate and trench geometries, we examine large and small plate sizes of 54° and 36°, both for square subducting plates ($L = W$). Additionally, we separately vary plate width W, with large and small values of 36° and 54°, while holding the plate length constant at 45°. We also vary parameters related to the rear trench, including trench length (the relative size of the rear trench: T_2/T_1) and trench separation (the distance between the two trenches normalized by plate length: L_1/L). We examine large and small relative trench lengths of 2/3 and 1/3, respectively, and large and small trench separations of 1/2 and 1/6. We also vary the orientation of the inserted rear intra-plate trench relative to the fixed frontal trench. We examine rear-trench angles of 11°, 22°, and 31°, relative to the parallel-trench reference case of 0°. Such variable trench-trench angles, relative to the parallel trench cases, result in varying degrees of oblique convergence at the rear intra-plate trench.

To investigate how multiple geometric factors may interact, we conducted two extended tests designed to explore combinations of plate parameters. These tests are not intended to be exact reconstructions of a specific region. Instead, they are simplified models based on the main features of the Neo-Tethys system during the Late Cretaceous (Gürer et al., 2022; van Hinsbergen et al., 2020). For example, the complex 'saw-tooth' segmented trench geometry is simplified into two variables: trench obliquity and separation distance. In Model M_1, obliquity is fixed at 31° while plate size ($L = W$) is increased further to 60° (~6,600 km). This is to test how obliquity affects the plate velocity in larger plate cases. Model M_2 maintains the same large plate size and 31° obliquity as M_1, but contains a lower trench separation (L_1/L) of 1/6 relative to 1/3. This allows us to evaluate how reduced trench separation influences plate velocity in a large-scale, oblique system. Full model parameters are listed in Table S1 in Supporting Information S1.

2.4. Numerical Parameters

We employ a non-uniform mesh resolution to simultaneously resolve both lithospheric deformation and mantle-scale circulation. The mesh is refined in regions with large viscosity gradients and within the prescribed compositional domains, allowing high resolution within the lithosphere while simultaneously capturing large-scale mantle flow. The refinement strategy produces a maximum refinement corresponding to ~2.8 km radially thick finite elements (in the lithosphere and crust) and a minimum refinement corresponding to ~45 km thick elements (lower mantle). This results in ~4,900,000 cells, distributed non-uniformly across the domain. All simulations were performed on the Skylake (SKX) nodes of the Texas Advanced Computing Center's Stampede3 supercomputer.

2.5. Velocity Analysis Method

To isolate the impact of the second slab on plate motion, we compare equivalent single and double subduction models. Horizontal plate velocities are extracted 20 km below the surface, deep enough to lie beneath the highly deformed crustal layer and thus unaffected by near-surface deformation. We analyze both the ratio of velocity magnitudes (e.g., the shading in Figure 2a) and the differences in velocity vectors (arrows in Figure 2a). Rather than plotting raw differences, all values are normalized by the corresponding single subduction velocity field. This normalization removes the absolute velocity variations that arise for different rheological parameters, thereby highlighting the relative effect of the second trench.

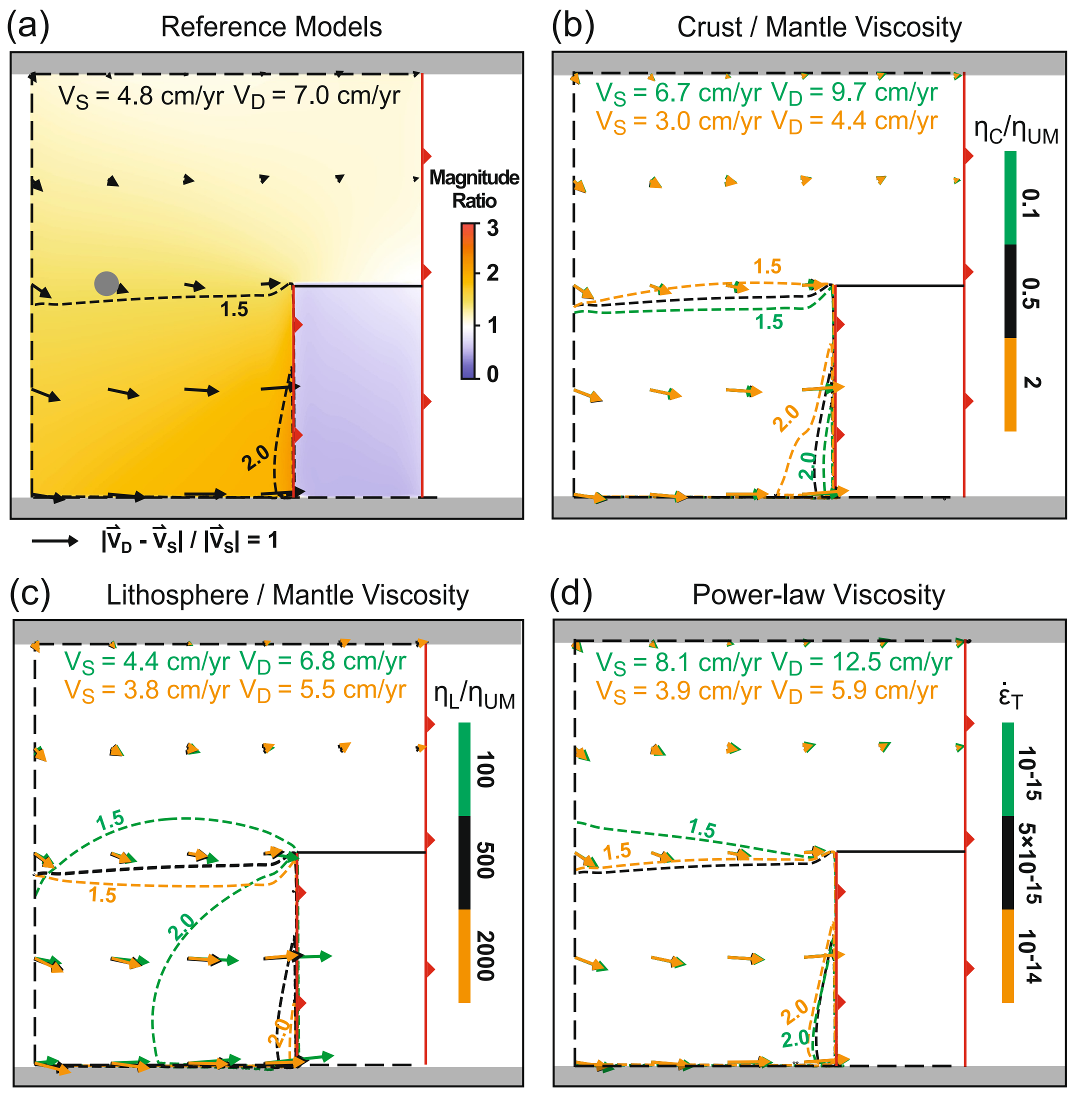

Figure 2. (a) Velocity magnitude ratio, expressed as the double to single subduction plate velocity ratio, for the reference models. Arrows show velocity-difference vectors normalized by the local single subduction velocity, $(V_D - V_S)/|V_S|$. The gray dot marks the fixed far-field reference point within the interior of the subducting plate, where velocities are extracted for comparison among models. V_S and V_D indicate the absolute velocities at this reference point in the single and double subduction models, respectively. Black contours indicate magnitude ratios of 1.5 and 2 in the reference models. The other panels display velocity-difference vectors and contours of the magnitude ratio for pairs of models with variable (b) crust/mantle viscosity ratio, (c) lithosphere/mantle viscosity ratio, and (d) transition strain rate. Green and orange denote the low and high values of each variable, respectively.

We also determine the best-fitting Euler pole of the subducting plate. This allows us to characterize the velocity field as a rigid-plate rotation on a sphere. Euler pole positions are identified using a least squares optimization that minimizes the misfit between velocities predicted by rigid-plate rotation and those obtained from the numerical model (e.g., Figure 3a). The misfit is defined as the normalized root-mean-square (RMS) difference:

$$V_{\text{Misfit}} = \frac{\Delta \mathbf{V}_{\text{rms}}}{\mathbf{V}_{\text{rms}}} = \frac{\sqrt{\frac{1}{N} \times \sum_i |\mathbf{V}_{\text{Model},i} - \mathbf{V}_{\text{Pre},i}|^2}}{\sqrt{\frac{1}{N} \times \sum_i |\mathbf{V}_{\text{Model},i}|^2}} \quad (5)$$

where N is the number of velocity samples, i denotes each point at which velocities are extracted, $\mathbf{V}_{\text{Model}}$ and $\mathbf{V}_{\text{Pre}}$ are velocity vectors in the numerical models and rigid plate predictions, respectively. Velocities are uniformly

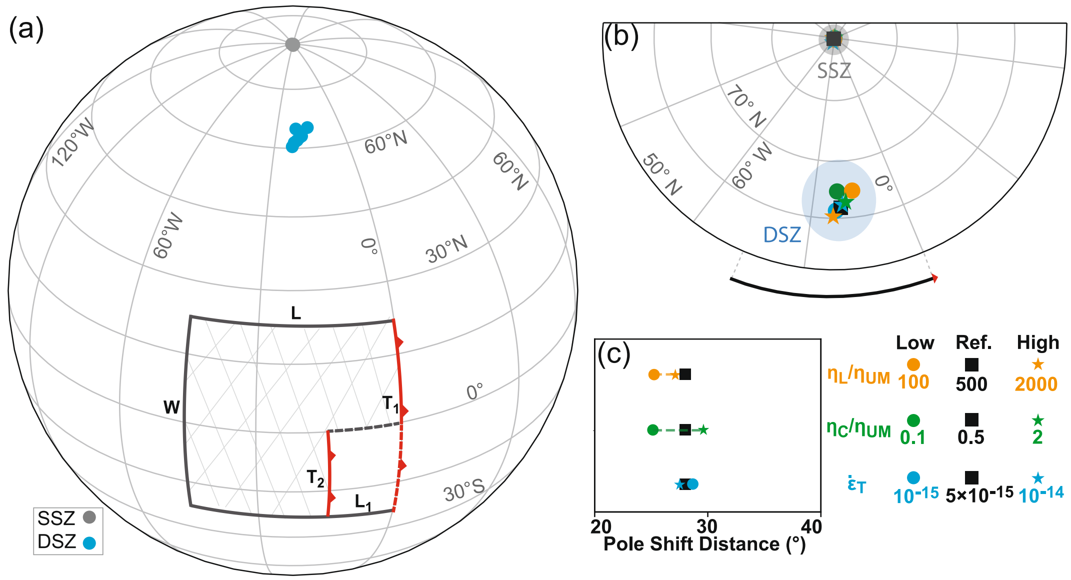

Figure 3. (a) Best-fitting Euler pole positions for single subduction (gray) and double subduction (blue) models with varying rheologies. (b) Zoomed-in view of the double subduction Euler pole positions, distinguished by symbol, and color; black curves and red arrowheads denote the reference subducting-plate extent. (c) Great-circle Euler pole shifts between each single and double subduction model pair.

sampled over the points of a $1^\circ \times 1^\circ$ grid, which is sufficient to capture the large-scale rigid-plate signal; denser sampling produces only minor differences in the inferred Euler pole. From this calculation, we can also determine the plateness (P), which quantifies the degree to which modeled plate velocities follow those of the rigid rotation about the best-fitting Euler pole, as $P = 1 - V_{\text{Misfit}}$ (Liu & King, 2022; Mallard et al., 2016; Zhong et al., 1998). A plateness of 1 indicates a perfectly rigid plate, whereas lower values reflect increasing internal deformation. The intervening segment between the two trenches is excluded because the intra-plate weak zone inserted into the double subduction models causes it to decouple and behave as an independent plate. After determining the Euler poles for pairs of single and double subduction models, we quantify the shift by calculating the great-circle distance between the two poles (e.g., Figures 3c and 4c).

2.6. Torque Balance

To understand the physical drivers of the numerically modeled subducting plate velocities, we investigate the extent to which a torque balance between slab pull and basal drag can reproduce these velocities. We subsequently compare the Euler poles predicted by the torque balance with those fitted to the numerical model velocity fields, which enables us to isolate the primary geodynamic controls on plate motion in the more complex numerical models. As with the Euler pole fit to the numerically modeled plate motions, the torque-balance solution is constrained to rigid rotation of the subducting plate on a sphere, defined by three parameters: Euler pole latitude, longitude, and rotation rate. We identify the rigid-plate rotation for which the basal-drag torque, computed from the corresponding rigid-plate velocity field, most closely balances (i.e., is equal in magnitude and opposite in direction to) the slab-pull torque.

The slab-pull torque ($\mathbf{T}_{SP}$) is computed by integrating the local torque contributions, from the trench-perpendicular slab-pull force per unit trench length, along the trench (e.g., Faccenna et al., 2012). The magnitude of slab-pull force per unit length $\left(\mathrm{f}_{SP}\right)$ is taken as:

$$\mathrm{f}_{SP} = \Delta\rho g H_{sp} L_{sp} \sin(\alpha) \tag{6}$$

where $\Delta\rho$ is the density contrast between slab and surrounding mantle, H_{sp} is the slab thickness, L_{sp} is the slab length, and α is the slab dip.

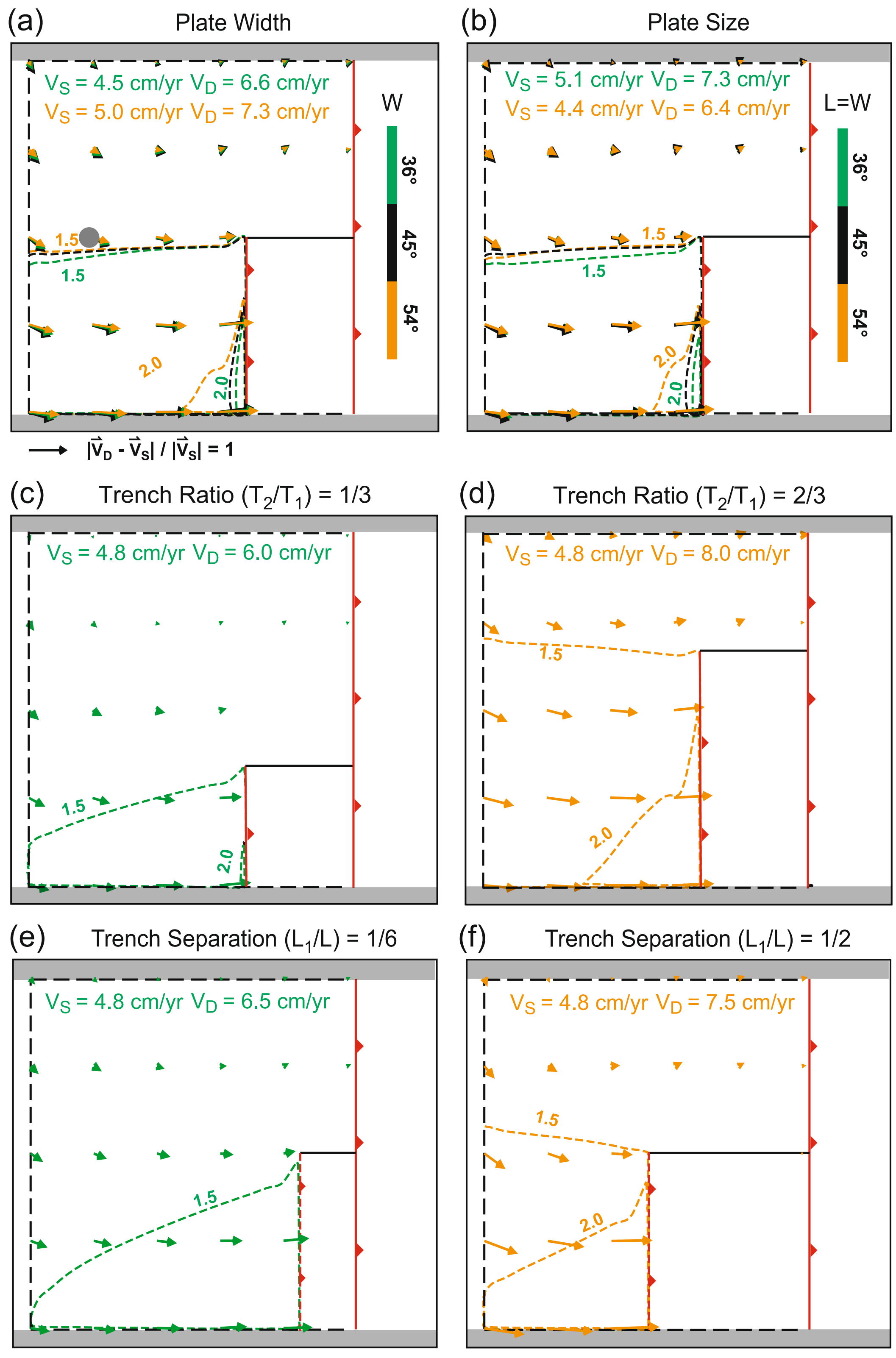

Figure 4. Similar to Figure 2, the panels display velocity difference vectors and contours of the magnitude ratio for pairs of models with variable (a) plate width and (b) plate length. Panels (c and d) show low and high values of trench length ratio, respectively, while panels (e and f) display low and high values of trench separation.

The total slab-pull torque (Figure S2b in Supporting Information S1) is then obtained as the trench-length (L_{trench})-integrated cross product between the position vector $\mathbf{r}$, measured from the planet's center, and the local force element $(d\mathbf{f}_{SP})$:

$$\mathbf{T}_{SP} = \int_{L_{\text{trench}}} d\mathbf{T} = \int_{L_{\text{trench}}} \mathbf{r} \times d\mathbf{f}_{SP} \tag{7}$$

As also illustrated in Figure S2c in Supporting Information S1, the opposing basal-drag torque $(\mathbf{T}_{BD})$ is evaluated by integrating the viscous shear stress over the area of the subducting plate (Iaffaldano & Bunge, 2015):

$$\mathbf{T}_{BD} = \iint_A \mathbf{r} \times d\mathbf{f}_{BD} \tag{8}$$

Here, $d\mathbf{f}_{BD}$ is the local basal shear force acting on the plate–mantle interface, which depends on the plate velocity ($\mathbf{v}$), the elemental plate area (dA), the assumed basal shearing thickness (H_{sh}), and mantle viscosity (η):

$$d\mathbf{f}_{BD} = \eta \frac{\mathbf{v}}{H_{sh}} dA \tag{9}$$

For simplicity, the shearing thickness and viscosity are held constant at 100 km and 2×10^{20} Pa s, respectively, for all semi-analytical calculations, rather than being adjusted for each single–double subduction parameter case. This globally constant viscosity allows us to isolate the first-order effects of slab-pull geometry and effective plate area on the torque balance. Note that the slab-pull torque is set entirely by the imposed slab geometry and is independent of the three rotation parameters, whereas the basal-drag torque is proportional to the local plate velocity and therefore varies with the Euler pole position and rotation rate.

In the single subduction reference case, slab pull is integrated along the full frontal trench (Figure S2d in Supporting Information S1). In the double subduction configuration, the inserted rear trench removes the slab-pull contribution from part of the frontal trench, shown as the dashed segment in Figure S2e in Supporting Information S1, while adding a second slab-pull contribution from the rear slab. The total slab-pull torque is therefore calculated as the sum of the frontal- and rear-trench contributions (Figure S2e in Supporting Information S1). To account for possible force transmission between the two same-dip slabs, we introduce a dimensionless parameter (k), such that the rear trench experiences an enhanced unit slab-pull force of $(1 + k)\mathbf{f}_{SP}$. This parameterization allows us to explore how inter-trench slab-pull transmission affects the torque balance; the sensitivity of the predicted Euler pole and rotation rate to this transmission-efficiency parameter k is examined in detail in Section 3.4. The second trench also partitions the subducting plate, changing the effective plate area from a quadrilateral to an L-shaped polygon and thereby redistributing basal drag and its associated torque (Figure 1c and Figure S2 in Supporting Information S1).

To determine the Euler pole location and rotation rate predicted by the semi-analytical torque balance, we perform a grid search over the three rotation parameters (Euler pole latitude, longitude, and rotation rate). For each candidate solution, we compute the rigid-plate velocity field and corresponding basal-drag torque. The solution minimizing the residual between the slab-pull and basal-drag torques defines the Analytical-EP and Analytical-Velocity shown in Figure 7, which are obtained entirely from the torque-balance calculation. Separately, the velocity field output from each numerical model is fitted with a rigid-plate rotation to obtain the corresponding best-fitting Euler pole (Numerical-EP in Figure 7); the model-output velocity field itself is labeled Numerical-Velocity. These numerical results are used only for comparison with the semi-analytical predictions and are not used as input to the analytical basal-drag calculation. This torque analysis allows us to test whether the numerically modeled velocity differences between single and double subduction models can be approximated by a simplified balance between slab pull and basal drag. In this torque balance, secondary contributions such as slab-bending resistance, complex mantle-flow effects, and ridge push are not included as separate torque terms. We note, however, that viscous resistance to plate/slab bending is still implicitly present in the full numerical models through deformation of the lithospheric layer, whereas elastic flexural stresses are not resolved because elasticity is not included. The torque analysis is therefore intended to isolate the primary driving mechanisms underlying changes in plate motion, rather than to provide a complete force decomposition.

10.1029/2026JB034505

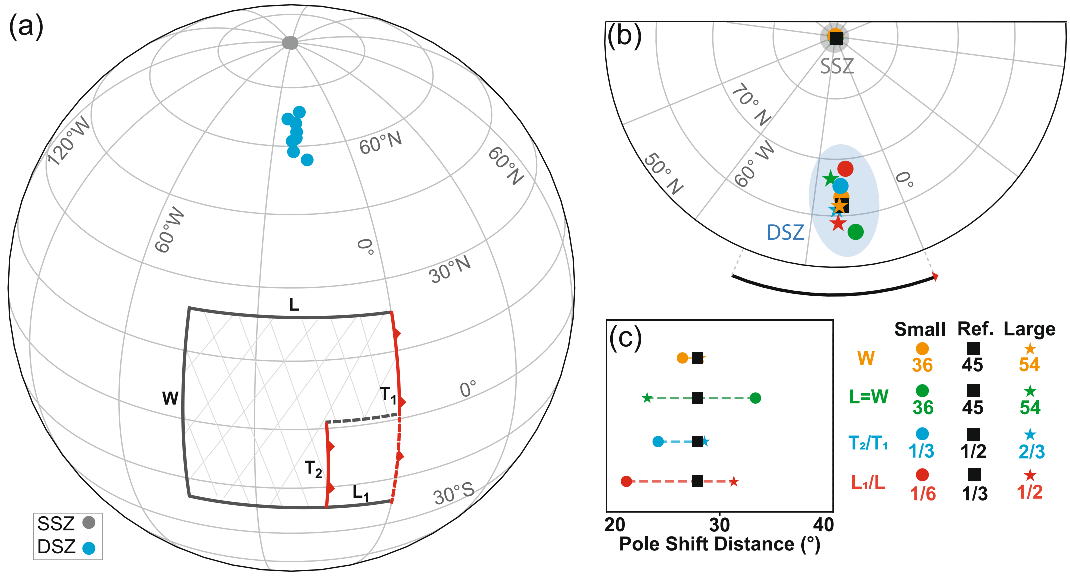

Figure 5. (a) Similar to Figure 3, the best-fitting Euler pole positions for models with varying plate and trench geometries, (b) the corresponding zoomed-in view, and (c) the resulting Euler pole shifts.

3. Results

We first compare the reference single and double subduction models, which establish the baseline velocity increase and Euler pole shift associated with double subduction. We then examine rheological variations as a robustness test: material properties set the absolute velocity scale, but should not alter the relative double-to-single response. Finally, we evaluate the plate and trench geometries, which directly modify the torque balance and exert the strongest control on relative velocity differences and Euler pole shifts.

3.1. Plate Velocities in the Reference Models

We first compare plate velocity fields between the reference single and double subduction models (Figures 1b and 1d). In the single case, plate velocity magnitude peaks at ∼7 cm/yr near the trench and averages ∼5 cm/yr in the far field. In the double subduction case, velocities increase to ∼8 cm/yr near the frontal trench and ∼10.5 cm/yr behind the rear trench. Far field plate velocities are also higher in the double subduction case; for example, at a representative far-field location (gray dot in Figure 2a), velocity increases from 4.8 cm/yr in the single model to 7.0 cm/yr in the double model, giving a ratio of 1.5. The velocity ratio (double/single) exceeds 1 throughout the subducting plate (Figure 2a). The ratio peaks at ∼2.3 directly behind the rear trench and decreases northward. The insertion of a second slab also redirects plate motion southeastward, as shown by the velocity difference vectors (Figure 2a). At the representative far-field location, there is a 6° angle between the single and double subduction velocity vectors in the reference cases; a complete list of these angular shifts across all models is provided in Table S2 in Supporting Information S1.

Although our models have a viscous lithospheric rheology, and hence permit internal deformation, the subducting plate behaves in a relatively rigid manner. That is, plate velocities have high plateness values of ∼0.92 (corresponding to normalized velocity misfits of ∼0.08, i.e., ∼8% deviation from rigid rotation) in both single and double reference cases (Figure S3 in Supporting Information S1), confirming that an Euler-pole representation is appropriate. These results align with the plateness of 0.93 reported in the spherical models of Liu and King (2022) and are higher than the global estimate of ∼0.87 from Earth's geodetic strain rate model (Kreemer et al., 2003), which also includes deforming plate boundary zones. Similar values are observed in most parameter tests, except in the weak-lithosphere cases $\left(\eta_L/\eta_M = 100\right)$ where a plateness of ∼0.8 indicates much greater intraplate deformation.

The best-fitting Euler poles reflect these plate velocity differences between single and double subduction. Because the single subduction model is north–south symmetric and centered on the Equator, its Euler pole is at the geographic North Pole. In the double subduction case, the Euler pole shifts southward by ∼30° (Figure 3a), and also shifts east of the longitudinal center of the plate by a more moderate ∼2°. The southward drift and eastward offset are consistent with, respectively, the increased plate velocities ahead of the double subduction section and the addition of a southward velocity component. The rotation rate around the best-fitting Euler pole increases from ∼0.44° Myr^{-1} in the single subduction case to ∼0.69° Myr^{-1} in the double subduction model, corresponding to a ratio of ∼1.57 (Table S3 in Supporting Information S1 for a full list of rotational rate ratios). This is consistent with the velocity magnitude ratio at the representative far-field point. Additional sensitivity tests with shallower and deeper imposed slab-tip depths (350 and 550 km) produce Euler pole positions within 1° of the reference 450-km slab-tip depth models, suggesting that the relative plate-motion response is only weakly sensitive to the imposed slab-tip depth (Figure S4 in Supporting Information S1).

3.2. Rheological Effects on Plate Velocities

We now describe the impact of varying crustal, lithospheric, and mantle viscosities within our pairs of single and double subduction models. Overall, these rheological parameters exert a strong control on the absolute speed of plate motion in both the single and double subduction models, but only modestly alter the relative impact of double subduction.

Crustal viscosity exerts a strong control on absolute plate velocity (Figure 2b). Compared to the reference models $\left(\eta_C/\eta_M = 0.5\right)$, where the far-field velocity in the double subduction case reaches 7.0 cm/yr, plate velocity is ∼40% lower in the strong crust case (4.4 cm/yr; $\eta_C/\eta_M = 2$), and ∼40% higher in the weaker case (9.7 cm/yr, $\eta_C/\eta_M = 0.1$). Despite this large contrast in absolute speeds, the double-to-single velocity ratios remain nearly identical across all cases. This can be seen by near-identical contour distributions of the double-to-single plate velocity ratio (Figure 2b) and a similar ∼6° azimuth difference at the far-field reference point (Table S2 in Supporting Information S1). This indicates that the crustal viscosity strongly impacts the overall plate speed but does not significantly affect the relative velocity differences caused by the addition of a second trench. Because the 15-km-thick crustal layer is resolved by only ∼5 elements at the reference resolution (∼2.8 km), we reran the reference model pair with a doubled crustal-layer resolution (∼1.4 km). This produces similar first-order velocity patterns, double-to-single velocity ratios, and Euler pole shifts (within 1°), supporting the robustness of the reference-resolution results (Figure S5 in Supporting Information S1).

Lithospheric viscosity similarly influences absolute plate speeds (Figure 2c). In models with stronger lithospheric plates $\left(\eta_L/\eta_M = 2000\right)$, the subducting plate has lower velocities in both the single and double subduction models, with 5.5 cm/yr at the far-field point in the double case. The weaker lithosphere cases $\left(\eta_L/\eta_M = 100\right)$ exhibit higher plate velocities overall, consistent with reduced viscous bending resistance at the trench. The area of the subducting plate undergoing enhanced relative acceleration (i.e., high double-to-single velocity ratios) extends farther into the plate interior than in the other two lithospheric strength cases. This is due to the enhanced intraplate deformation, as also recorded by its low plateness. However, the far-field velocity differences remain broadly similar (ratios of 1.4–1.6 and azimuth differences of ∼6–7°), indicating that changes in lithospheric strength primarily affect the region closely behind the trench where intraplate deformation is concentrated.

Mantle rheology, parameterized by the transition strain rate $\left(\dot{\epsilon}_T\right)$ in our models, similarly scales plate velocity magnitudes without significantly affecting the velocity differences between double and single subduction (Figure 2d). A lower transition strain rate (10^{-15} s^{-1}), which results in more dislocation creep and a reduced effective mantle viscosity, increases plate velocities by 79% at the far-field reference point. Conversely, a higher strain rate (10^{-14} s^{-1}) reduces plate velocities by ∼16%. Crucially, the velocity ratio (∼1.5 at the far-field point) and azimuth difference (∼6°–7°) between the double and single cases again exhibit only minor variations as a function of mantle strength.

The changes in Euler pole positions cluster within a relatively small region for all model pairs (Figure 3a). While equatorial symmetry of the single subduction zone situates all poles at the North Pole, the addition of a second slab shifts the poles southward by 25°–30° across all double subduction cases (Figures 3a and 3b). In detail, there is ∼3° of variation in the Euler pole shift distance for the variable crustal viscosity cases, ∼5° for the variable lithospheric strength cases, and only ∼1° for the variable mantle strength cases (Figure 3c). Similarly, the single-to-double subduction ratios of Euler pole rotation rates are relatively constant, between 1.54 and 1.61, for all tests.

3.3. Geometric Effects on Plate Velocities

Having established that the relative double-to-single velocity differences are broadly robust across rheological variations, we next examine the geometric parameters that directly modify the torque balance and dominate the resulting Euler pole shifts. To compare models with different plate sizes, we normalize the plate coordinates by the plate length and width, so that each plotted point represents an equivalent relative position within the subducting plate. At each position, we calculate the velocity-difference vector between the double and single subduction models and normalize its magnitude by the local single subduction velocity. Figure 4 therefore shows normalized relative velocity differences on a normalized plate geometry, rather than absolute velocity differences.

The relative plate velocity differences remain consistent when plotted in non-dimensional coordinates, regardless of variations in plate width or overall plate size (i.e., both width and length). That is, the normalized velocity difference vectors and velocity ratio contours are relatively insensitive to plate width-only and overall plate size variations (Figures 4a and 4b). However, because these comparisons are made in normalized plate coordinates, they reflect relative spatial patterns rather than the absolute velocity distribution on the sphere. The absolute velocity distribution in double subduction models is highly sensitive to plate size, and velocity vectors for small and large plates differ significantly at the same geographic locations (Figure S6b in Supporting Information S1). In contrast, the double subduction velocity fields are very similar when only plate width is varied (i.e., length held constant; Figure S6a in Supporting Information S1). Consequently, the best-fitting Euler poles shift substantially with changes in plate size: smaller plates undergo larger Euler pole displacements (∼33°), while larger plates exhibit reduced shifts (∼24°). By contrast, the Euler pole shift remains nearly constant for variable plate widths, at 27°–28° (Figure 5).

The trench length ratio (T_2/T_1), which defines the relative length of the intra-oceanic trench, exerts a substantial influence on both plate velocity patterns and Euler pole shifts. Models with shorter intra-oceanic trenches ($T_2/T_1 = 1/3$) exhibit a modest speedup (a ratio of 1.25) over a limited spatial extent. In contrast, larger ratios ($2/3$) produce a greater speedup (ratio of 1.67) over a broader area (Figures 4c and 4d). This is accompanied by an increase in the rotation-rate ratio, between the best-fitting single and double subduction Euler poles, which rises to 1.79 compared to 1.34 in the small T_2/T_1 model. Euler pole shifts are less sensitive to this variable than to plate size and range between 25° and 29°.

The relative separation between the two trenches also exerts a strong control on plate velocity patterns and Euler pole displacement. With greater separation ($L_1/L = 1/2$), the effective subducting plate area behind the rear trench is reduced, producing a wider region of pronounced speedup behind the rear trench (Figure 4f), Euler pole displacements of ∼31°, and rotation rate ratios of 1.65. By contrast, with a smaller separation ($L_1/L = 1/6$), the speedup is reduced such that none of the plate has a velocity magnitude ratio above 2 (Figure 4e), and the Euler pole shift decreases to ∼22° (Figure 5c), with the rotation rate ratio decreasing to 1.42.

Trench obliquity further modifies both the plate velocity patterns and the associated changes in Euler pole positions. With increasing obliquity, velocity vectors tilt progressively southward, from 6° to 13° at the representative far-field location (Figure 6a). Increasing obliquity therefore produces progressively larger eastward Euler pole shifts, of up to 17° (Figure 6b). Furthermore, our extended tests explore combined effects: in Model M1, with plate size increased to 60° and trench obliquity of 31°, the Euler pole lies ∼8.5° closer to the pole position of the corresponding single subduction case. In Model M2, where trench separation is reduced to 1/6, the Euler pole displacement decreases to 14° (Figure 6b).

Overall, geometric variables exert a more pronounced influence on Euler pole displacements than the rheological variables. In particular, parameters that modify plate and trench geometry, including plate size, trench separation, and obliquity, drive significant Euler pole shifts. Conversely, absolute plate speeds are less sensitive to the tested range of geometric variables than to the rheological variations.

3.4. Torque Balance

We now evaluate whether the numerically modeled plate velocities and Euler pole positions can be predicted using a balance between the slab-pull and basal-drag torques (Figure 7). As detailed in the Methods and Figure S2 in Supporting Information S1, the slab-pull torque is calculated by integrating the slab-pull force along the trenches, whereas the opposing basal-drag torque is calculated by integrating the plate-velocity-dependent basal shear force over the effective plate area. The Analytical-EP is the Euler pole predicted by this torque balance

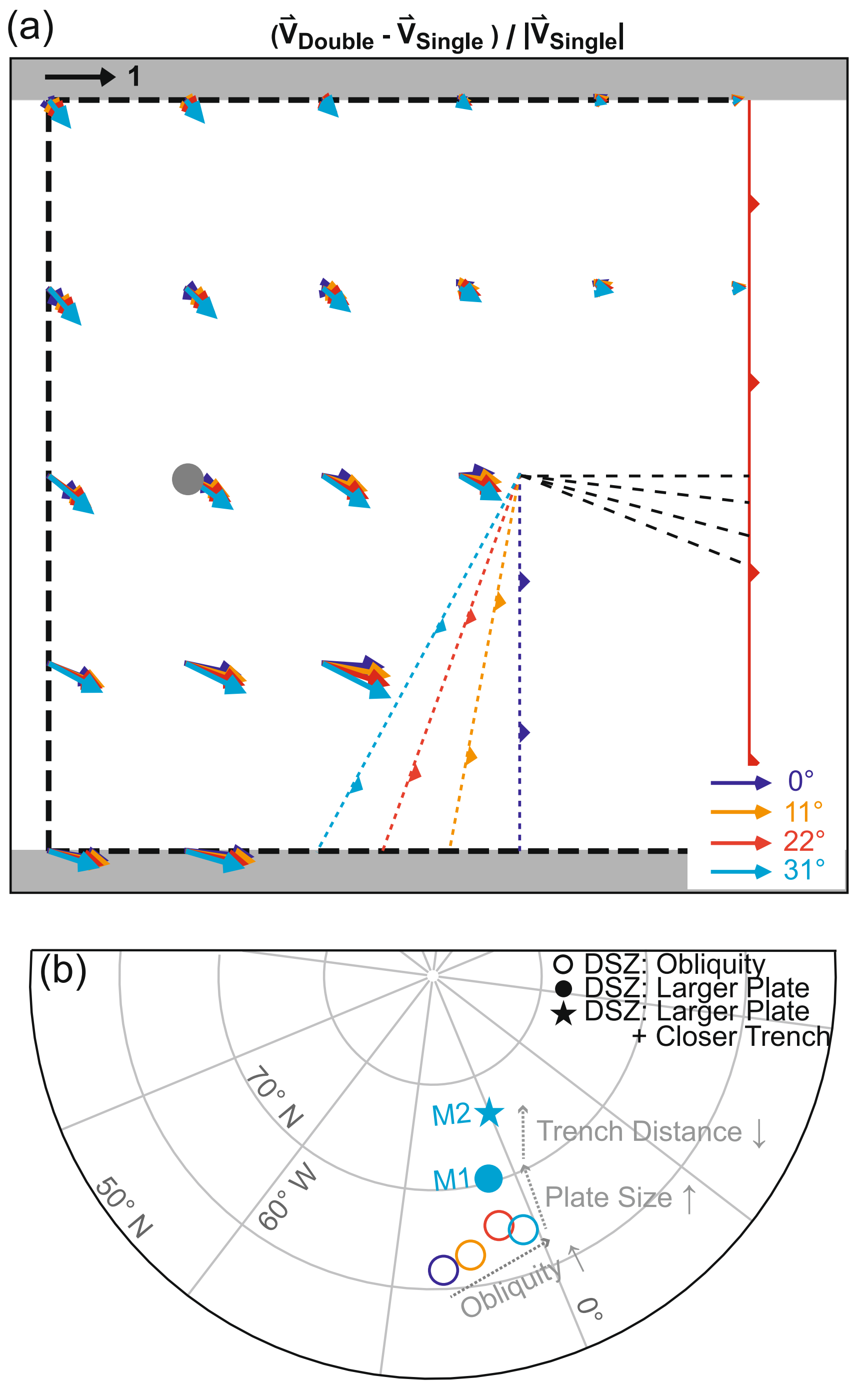

Figure 6. (a) Normalized velocity difference vectors for double subduction models with varying obliquities of the second trench (dashed lines), with the obliquities displayed in different colors. The dashed black lines are the corresponding weak zones that are perpendicular to the trenches. (b) Zoomed-in views of Euler poles in models with increasing obliquity (left to right), with the final two markers showing modifications to the 31° obliquity case: increased plate size (M1) and reduced trench separation (M2).

alone; the Numerical-EP is fitted to the numerical model velocity field and is used only for comparison (Section 2.6).

In the single subduction case, the symmetric trench geometry produces a north-directed slab-pull torque balanced by a south-directed basal-drag torque (Figure S2a in Supporting Information S1). In the double subduction case,

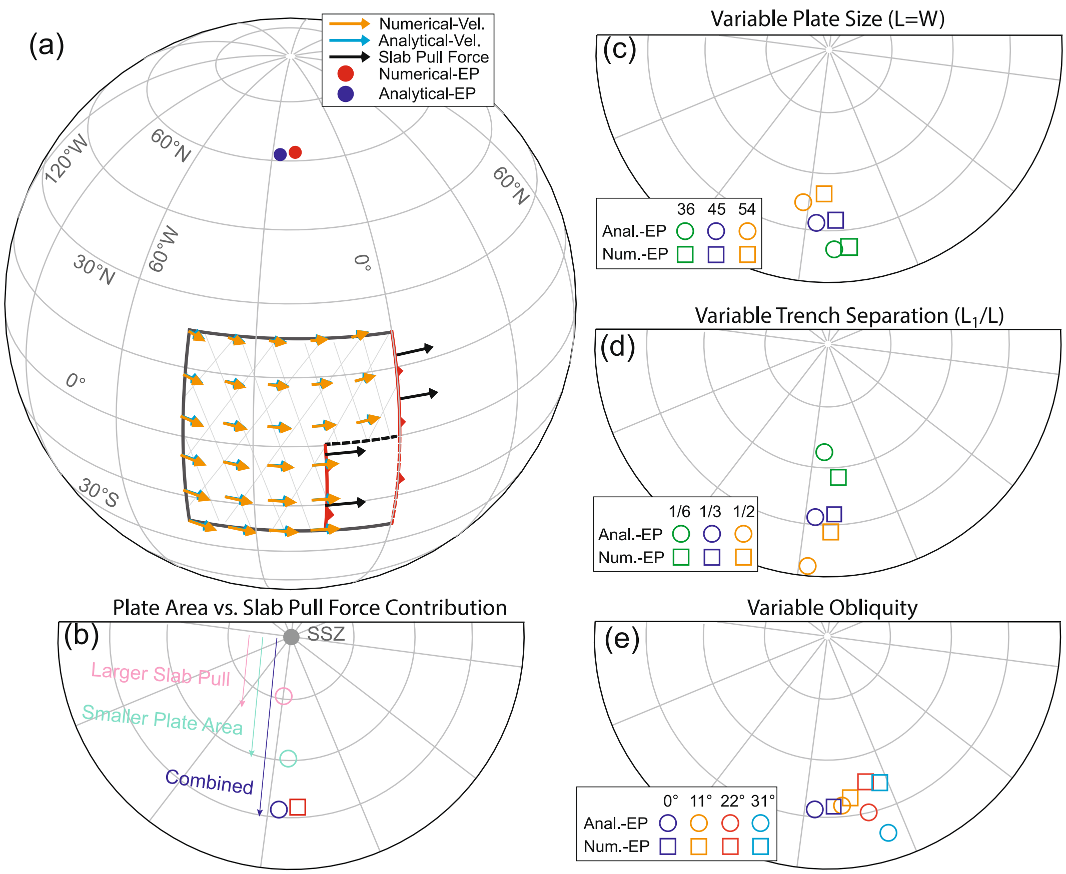

Figure 7. Analysis of Euler pole (EP) displacements and torque-balance predictions in double subduction systems. (a) Comparison between numerical model results and semi-analytical torque-balance predictions for the reference double subduction case. Numerical-velocity denotes the original model-output velocity field, from which the best-fitting numerical-EP is computed. Analytical-EP denotes the Euler pole predicted independently from the torque-balance calculation, and analytical-velocity denotes the corresponding velocity field. The velocity vectors are shown to compare the original numerical model-output velocity field with the torque-predicted (analytical) plate velocity field. (b) Torque-based decomposition of EP shifts from the single subduction baseline (gray circle): the shift caused by changing slab-pull torque from the single to double subduction configuration while keeping the single subduction effective plate area (pink), the shift caused by changing effective plate area while keeping the single subduction slab-pull torque (cyan), and the combined effect of both changes (blue). The numerical-EP (red square) is plotted for comparison with the analytical torque-balance prediction. (c–e) Comparison between numerical-EP and analytical-EP positions for models with variable (c) plate size, (d) trench separation, and (e) rear-trench obliquity.

slab pull is applied at two trenches, producing two torque contributions with different orientations and lever arms relative to Earth's center. In the reference model, the addition of the rear trench modifies the magnitude and orientation of the net slab-pull torque, forcing the plate to reorganize its velocity field so that the basal-drag torque ($\mathbf{T}_{BD}$) again balances this modified driving torque. The efficiency of force transmission between the two trenches is parameterized by the dimensionless factor k, which sets the fraction of frontal slab-pull force transmitted through intervening plate segment (i.e., from the front to the rear trench). We adopt a constant value of $k = 0.15$, which represents the transmission of 15% of the frontal slab pull $(\mathbf{f}_{SP})$ to the rear trench, as it reproduces the numerically derived Euler pole shift for the reference model pair.

Using this transmission factor, the semi-analytical torque balance reproduces the ~28° Euler pole displacement in the reference model (Figure 7b). To quantify the relative contributions of subducting plate geometry and slab-pull force, which both change in the transition from single to double subduction, we performed two simplified end-member analytical tests in which one factor was varied while the other was fixed to the single subduction reference. In the first test, the plate area was reduced to that of the double subduction geometry (A_D) while the slab-pull torque ($\mathbf{T}_{SP}$) was fixed to that of the single subduction setup. This yielded a ~20° pole shift due solely to the reduction in effective plate area behind the inserted trench (Figure 7b). In the second test, the slab-pull force was increased and redistributed to the double subduction configuration $((1 + k)\mathbf{f}_{SP})$, while the subducting plate geometry remained fixed to that of the single subduction case (A_S). This produced a ∼10° shift in the Euler pole location. These results indicate that, for our reference configuration, the reduction of plate area behind the rear trench contributes more to the Euler pole shift than the additional and redistributed slab pull force due to double subduction. Together, the combined contributions (∼30°) align with the total ∼28° observed in the reference double subduction model (Figure 7b), demonstrating that these two factors drive the numerically modeled Euler pole shifts.

Keeping $k = 0.15$ fixed, the analytical torque balances reproduce the first-order Euler pole shifts for our other geometric tests. Torque calculations were not performed for the plate width and trench length ratio tests, as their Euler-pole shifts are less pronounced. Increasing the plate size progressively shifts the double subduction Euler Pole northwestward, as numerically modeled, thereby reducing the Euler pole displacement (Figure 7c). Decreasing trench separation reduces the primarily latitudinal Euler pole shift, although this is less well matched by the analytical torque balances (Figure 7d). Increasing trench obliquity causes the Euler poles to migrate eastward in the numerical models; while the analytical calculations capture this longitudinal trend, they do not reproduce the southward shift also observed in the numerical models (Figure 7e). Hence, while a constant transmission factor of $k = 0.15$ enables us to analytically match the first-order pole-shift trends for most of the tests, discrepancies arise for certain models. These deviations suggest that a uniform k may be overly simplistic for certain geometries. The factors that may contribute to these mismatches, and comparisons with variable transmission factors, are addressed in the Discussion.

4. Discussion

4.1. Mechanism of Velocity Changes and Euler Pole Shifts

Slab pull is well established as the primary driver of plate motion, and Euler pole positions are dynamically determined by the instantaneous balance between driving and resisting torques (Coltice et al., 2019; Conrad & Lithgow-Bertelloni, 2002; Forsyth & Uyeda, 1975; Lithgow-Bertelloni & Richards, 1998). While large-scale mantle buoyancy structures evolve over ∼100 Myr, recent high-resolution marine magnetic and geodetic studies reveal plate motion variations occurring on shorter timescales, for example over just a few million years (e.g., Bull et al., 2010; Merkouriev & DeMets, 2014). Previous research suggests these changes can be triggered by variations in plate-boundary or slab-related forces, such as the initiation or cessation of subduction zones (Copley et al., 2010; Faccenna et al., 2012; Iaffaldano et al., 2006; Richards & Lithgow-Bertelloni, 1996), slab buckling (van der Wiel et al., 2024), or slab detachment (Bercovici et al., 2015). However, most studies focus on specific regions or single subduction systems; consequently, the kinematic consequences of double subduction, especially the impact of newly initiated intra-oceanic trenches on Euler pole position and plate rotation, remain poorly constrained.

Existing 2-D and limited-extent 3-D models of same-dip double subduction demonstrate that, relative to single subduction, additional slab pull is a primary driver of plate acceleration (e.g., Faccenna et al., 2018; Holt et al., 2017; Jagoutz et al., 2015; Pusok & Stegman, 2019, 2020). Crucially, the degree to which this additional slab pull is transmitted between subduction zones, and hence influences plate kinematics, depends on the efficiency of force transmission through the intervening plate (Holt et al., 2018; Jian et al., 2023). Our results build on these studies by showing that the finite lateral extent of the rear trench, characteristic of natural intra-oceanic systems, introduces an additional control on plate motion. Such finite rear-trench extent produces non-uniform plate velocities and associated plate motion re-orientations that cannot be fully captured by 2-D models or by 3-D models in which the rear trench extends across the full plate width. Because plate motions on a sphere are described by rotations around Euler poles, characterizing how these poles migrate is essential for linking double subduction-induced kinematic changes to tectonic and marine magnetic constraints (e.g., DeMets et al., 2010; Gürer et al., 2022; Torsvik et al., 2012; van Hinsbergen et al., 2020).

Our results indicate that the kinematic effect of same-dip double subduction cannot be interpreted simply as a direct consequence of additional slab pull. Previous studies have emphasized slab-pull transmission between two same-dip slabs as the main cause of plate acceleration, and our models support the importance of this mechanism. However, the torque-balance analysis shows that finite rear-trench geometry also modifies the resisting side of the

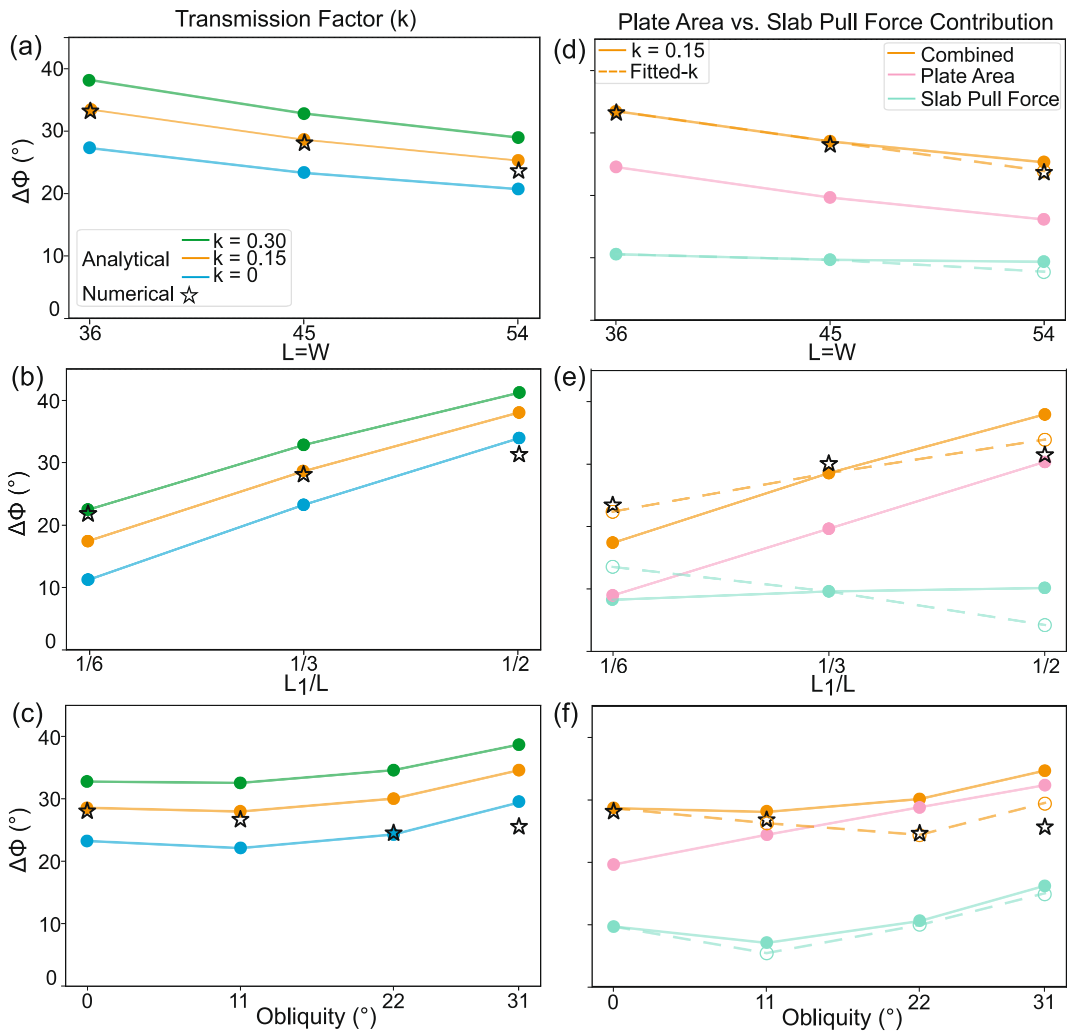

Figure 8. Euler pole shifts as a function of (a, d) plate size ($L = W$); (b, e) trench separation (L_1/L); (c, f) obliquity. Panels (a–c) show results for varying force transmission factors: $k = 0$ (blue), 0.15 (orange), and 0.3 (green). Panels (d–f) show results at a constant $k = 0.15$, with curves representing the individual contributions of reduced plate area (pink), additional slab pull force (cyan), and the combined effect (orange). Stars denote the corresponding numerical Euler pole shifts. Dashed curves show fitted k values that better match the numerical Euler pole shifts.

force balance by reducing the effective subducting-plate area contributing to basal drag. This reduction decreases the area over which resisting basal shear is integrated, allowing finite rear-trench systems to produce both acceleration behind the rear trench and substantial Euler pole migration. In the reference model, this reduced effective plate area contributes more to the Euler pole shift than the increase in net slab pull, highlighting the importance of basal-drag redistribution in intra-plate SDDS systems. Together, these two mechanisms explain the modeled double-to-single subduction velocity differences and Euler pole migration (Figure 9). More broadly, they suggest that natural episodes of intra-oceanic subduction initiation or termination may reorganize plate motion not only by changing slab-pull forces, but also by modifying the geometry of basal-drag resistance.

4.2. Dependence on Mechanical and Geometric Variables

Having established that plate acceleration and Euler pole migration arise from changes in slab pull and effective plate area, we now discuss how variations in rheological and geometric parameters influence this reorganization. Our results demonstrate that, while the absolute speeds of subducting plates within both single and double subduction systems are highly sensitive to rheological properties, the relative reorganization of their motion induced by double subduction is more sensitive to the geometry of the subduction system. Rheological

10.1029/2026JB034505

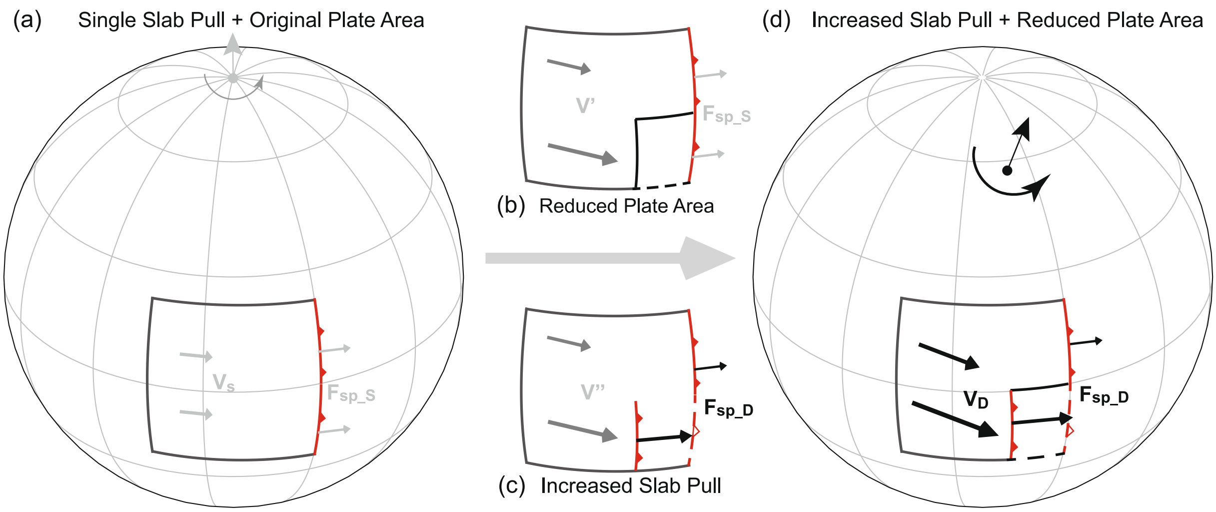

Figure 9. Illustration of the influence of same-dip intra-oceanic double subduction on plate velocity changes and the corresponding Euler pole shifts. The velocity difference between the single subduction case (a) and the double subduction case (d) can be decomposed into two primary drivers: (b) reduced effective plate area and (c) increased slab pull force. Changes in slab pull and plate velocity are indicated by varying arrow size and direction.

parameters, such as the viscosities of the plate interface and the surrounding mantle, strongly impact absolute plate velocities. For instance, a weaker crustal layer reduces the plate motion-resisting shear stresses along the plate interface and thereby increases plate speeds (e.g., Behr & Becker, 2018; Conrad & Hager, 1999), while a lower transition strain rate promotes non-Newtonian, power-law creep that increases plate speeds by reducing basal tractions below the plates (e.g., Holt & Becker, 2016; Jadamec & Billen, 2010). However, because the driving slab-pull torque remains consistent across model pairs with varied rheological parameters, the relative kinematic response to double subduction, specifically Euler-pole positions and velocity magnitude ratios, remains comparatively unchanged. By contrast, variations in plate and trench geometry modify the torque balance itself, thereby altering both the magnitude and direction of plate motion, including the position of the best-fitting Euler pole.

This geometric sensitivity arises because plate motion reflects the balance between slab pull acting along the trench and the basal drag resisting motion over the plate area. When the overall plate size increases (i.e., both W and L increase), slab pull continues to scale with trench length, but the redistribution of the resisting torque over the larger plate requires a more pronounced reorganization of the velocity field to reestablish torque balance. Consequently, significant changes in Euler pole position occur. By contrast, when plate width (W) is varied while plate length (L) is held constant, both the driving slab pull force (which scales with trench length) and the resisting basal-drag force (which scales with plate area, $W \times L$) increase proportionally. Because these torques scale together, the overall torque geometry remains similar, and only minor variations in absolute speed or Euler pole position arise.

Besides plate size, plate velocity distributions are also influenced by the location of the added trench. Positioning the added subduction zone farther from the frontal trench (i.e., a larger trench separation) reduces the effective basal area of the subducting plate that participates in resisting torque behind the rear trench. Previous modeling of single subduction systems with variable plate lengths demonstrated that reducing the effective plate area decreases basal drag resistance and promotes faster plate motion (e.g., Bellahsen et al., 2005; Holt & Becker, 2016; Xue et al., 2020). For example, shortening the subducting plate in the trench-normal direction reduces the area over which basal drag is integrated, allowing comparable slab pull to drive faster plate motion. On Earth, possible links between paleo-plate size and plate speed are consistent with this effect, most notably the ultra-fast motion of the Izanagi plate as it progressively shortened before being fully subducted (Müller et al., 2016; Wu et al., 2024). By analogy, in the double subduction configuration, greater trench separation reduces the portion of the plate that contributes to resisting torque, thereby enhancing the velocity increase associated with the second slab and producing larger Euler pole shifts. Increased trench separation also relieves the dynamic pressure buildup associated with the mantle trapped between the slabs, which would otherwise resist convergence (Holt et al., 2017; Jagoutz et al., 2015; Pusok & Stegman, 2019).

Journal of Geophysical Research: Solid Earth 10.1029/2026JB034505

Trench separation and overall plate size together determine the extent of the intervening segment between the two trenches. Within this region, transmission of slab pull from the frontal to the rear trench is subject to dissipation, manifested in our viscous models as distributed deformation of the intervening plate and, in natural systems, potentially as rifting or back-arc spreading (Holt et al., 2017; Jian et al., 2023). We parameterize this process using a transmission efficiency factor (k), which sets the fraction of the frontal slab-pull force transmitted to the rear trench. Our analytical results show that the predicted Euler pole shifts are highly sensitive to the magnitude of this force transfer. For variations in overall plate size, a constant transmission factor ($k \sim 0.15$), calibrated to the reference configuration, reproduces the numerical results well (Figures 8a and 8d). However, this same value does not reproduce all geometric trends, particularly for large trench separation and high obliquity (Figures 8b, 8c, 8e, and 8f). We therefore explored a range of k values to identify the optimal fit for each configuration (Figure 8a–8c). The best-fitting k values are geometry-dependent and decrease to near-zero for the large trench separation and high obliquity end-members. Because greater separation and obliquity correspond to increased distances between trenches, the decline in k indicates reduced slab-pull transmission efficiency as the intervening plate region expands.

Notably, even in the limit $k = 0$, the analytical model overpredicts Euler pole shifts for the largest trench separation and trench obliquity cases. A formal fit would thus require negative transmission efficiencies ($k < 0$), which are not physically meaningful. Rather than implying reverse force transmission, these negative values indicate that additional resisting torques are not fully captured in our simplified torque balances. In particular, by treating basal shear as the sole resisting torque and neglecting lithospheric bending dissipation (Buffett, 2006; Conrad & Hager, 1999), the analytical model likely overestimates the effective driving torque in these geometries. In addition, the semi-analytical torque balance assumes a constant basal viscosity for all models, whereas the numerical models include strain-rate-dependent mantle viscosity. A spatially uniform change in basal viscosity would rescale the predicted rotation rate in our torque balances without shifting the predicted pole position. The constant-viscosity assumption does, however, neglect lateral viscosity variations, which modify the basal-drag distribution and hence can shift the predicted pole position. Such variations arise in the numerical models through feedbacks between plate motion and dynamic asthenospheric weakening, which will reduce basal resistance beneath fast-moving plates (Lenardic et al., 2019; Patočka et al., 2024). This dynamic weakening is strongest beneath the fast-moving plate segment behind the rear trench, so accounting for it would reweight the basal-drag torque and could improve the analytical Euler pole predictions in exactly these largest-mismatch cases. However, incorporating such variations would require model-specific viscosity fields or additional scaling laws and would obscure the geometric torque decomposition that is central to our analysis. The inferred negative k values therefore act as a proxy for the resistive torques (e.g., plate bending) not included in the torque balances. Together, these simplifications mean that the analytical model is intended to capture the first-order torque balance rather than reproduce the full numerical solution. Importantly, across all configurations, including those with variable k, the reduction in effective plate area remains the dominant contributor to Euler pole shifts, with additional slab pull providing a secondary driver of Euler pole migration whose importance depends on the efficiency of trench-to-trench force transmission (Figures 8d–8f).

4.3. Geological Implications

Same-dip double subduction (SDDS) emerges from our models as an effective mechanism for reorganizing plate motion, capable of generating both acceleration and directional changes through torque redistribution. By altering effective plate area and modulating slab-pull transmission, SDDS provides a mechanical framework for interpreting several major plate-motion changes in Earth's history.

In the Neo-Tethys, plume-induced initiation of an intra-oceanic slab near Africa (van Hinsbergen et al., 2020) at ~105 Ma established a same-dip double subduction system whose developing slab pull between 96 and 92 Ma accelerated Africa from ~2–3 to 4.5–8 cm/yr and drove anticlockwise rotation, before ophiolite obduction and slab termination slowed the system at 85–70 Ma (e.g., Gürer et al., 2022). The modeled double-to-single velocity ratio near the newly initiated trench (up to 2.3 in the reference models) is consistent with the magnitude of the observed acceleration, supporting the inference that SDDS initiation can significantly increase subducting plate speed. The subsequent slowdown in the Neo-Tethys is also consistent with the reverse torque adjustment expected during SDDS termination. Farther east, the India–Eurasia system shows that double subduction can produce extremely high convergence rates. Although acceleration between 80 and 65 Ma has also been linked to the narrowing of the active trenches, and hence a reduction in inter-slab dynamic pressure buildup, the presence of a sustained double subduction system provided the mechanical framework to reach and sustain convergence rates exceeding 14 cm/yr (Jagoutz et al., 2015). This interpretation aligns with our numerical results, which show that double subduction configurations produce higher plate velocities than the single subduction cases across all tests. Specifically, the velocity magnitude ratio exceeds one across all tested configurations, reaching up to 2.3 directly behind the inserted trench. Conversely, the transition from SDDS to single subduction, following the demise of an intra-oceanic trench, may also produce significant plate motion variations through the inverse process: reduced slab-pull transmission and recovery of plate area diminish net driving torque and promote velocity reorganization. For example, the abrupt Pacific plate motion change marked by the ∼50 Ma Hawaii–Emperor seamount bend appears to coincide with termination of the Kronotsky subduction zone in the northwest Pacific Ocean (Clennett et al., 2023; Domeier et al., 2017; Hu et al., 2022; Konstantinovskaia, 2001; Vaes et al., 2019).

Our prescribed double subduction geometries are not intended to match a particular plate reconstruction, but to represent generic end-member configurations for exploring how an additional same-dip intra-plate subduction alters plate motion. While our models yield single-to-double subduction Euler pole shifts of up to 33°, geological reconstructions typically indicate changes of only a few degrees (e.g., Gürer et al., 2022). However, given our instantaneous modeling approach, these modeled shifts correspond to those between a single subduction zone and a mature double subduction system. Time-dependent modeling would be needed to investigate the timing of the transition to double subduction (Mishin et al., 2008; Pusok & Stegman, 2019), and of the associated Euler pole migration, but would introduce additional model complexity and parameters. Furthermore, our models M_1 and M_2 demonstrate that increasing obliquity, decreasing trench separation, and increasing plate size—complexities common in natural systems—substantially reduce these pole shifts, for example, to 14° in model M_2, which combines high obliquity, larger plate size, and reduced trench separation. Natural systems also involve additional driving forces, such as mantle plumes (e.g., Gerya et al., 2015; van Hinsbergen et al., 2021) and ridge push (e.g., Copley et al., 2010; Richardson, 1992), leading to kinematic mismatches with our simplified models. At the same time, geological reconstructions for regions like the Neo–Tethys often provide minimum estimates; because the seafloor fabric is lost, these reconstructions rely on net plate circuits that may overlook area gain from intra-oceanic extension, for example, the Eurasia–North America–Africa–Arabia plate circuit (e.g., Gürer et al., 2022; Seton et al., 2012). Thus, both model simplifications and the fragmented nature of the geological record contribute to the observed discrepancy.

Our interpretation of distance-dependent slab-pull transmission also provides a complementary mechanical perspective on the kinematic evolution of the Izu–Bonin–Mariana subduction system in the western Pacific. Ryukyu subduction has been proposed as the regional driver responsible for shifting the Izu–Bonin trench from retreat to advance (Faccenna et al., 2018; Čížková & Bina, 2015); however, although the Mariana trench is also advancing, its advance rate is substantially lower, approximately half that of the Izu–Bonin segment (Lallemand et al., 2008). Previous studies attribute this contrast to structural factors, proposing that although stress transfers efficiently from Ryukyu to Izu–Bonin, the Mariana back-arc basin dissipates transmitted slab pull, thereby limiting trench advance (Holt et al., 2018; Jian et al., 2023). Our results are consistent with reduced slab-pull force reaching the Mariana segment, but further suggest that geometric separation between trenches provides an additional control. In our framework, increasing trench-to-trench distance lowers transmission efficiency (k), even without explicit structural barriers, indicating that spatial separation itself can weaken slab-pull coupling. Thus, geometric distance, together with structural complexity, may explain why Mariana advance is more limited than farther north along the Izu–Bonin trench.

Although rheological parameters in convergent systems remain poorly constrained, including variations in lithospheric strength and mantle viscosity, and strongly influence absolute plate speeds, our results indicate that they exert comparatively minor control on the relative kinematic differences induced by double subduction when velocities are evaluated relative to single subduction reference states. Instead, geometric configuration emerges as the dominant control on plate acceleration and Euler pole migration. Because plate and trench geometries are directly constrained by tectonic reconstructions and are continually refined, this geometric sensitivity enhances the practical applicability of our framework. Incorporating region-specific geometric complexity into future models should therefore improve agreement between geodynamic model predictions and reconstructed plate-motion histories.

10.1029/2026JB034505

5. Conclusions

Our 3-D spherical geodynamic models demonstrate that intra-oceanic same-dip double subduction (SDDS) reorganizes the kinematics of large tectonic plates, accelerating them and systematically shifting their Euler poles. This is driven by a dual mechanism: the inserted rear trench partitions the subducting plate and thereby reduces the effective plate area contributing to basal-drag resistance, while additional slab pull provides an important but secondary contribution to plate velocity changes and Euler pole displacement. These effects are consistent across a wide range of tested parameters. Across these variations, we find that geometric variables (e.g., plate size and trench separation) primarily reorganize the distribution of driving and resisting torques, and thus control the relative plate velocity differences between single and double subduction, whereas rheological variables (e.g., plate and crustal strength) mainly control absolute plate speeds within both configurations. Furthermore, by comparing numerical models with analytical torque calculations, we show that the efficiency of slab-pull transmission between trenches within the SDDS configuration is distance-dependent, decreasing as trench separation increases. Overall, these findings support previous suggestions that the initiation or termination of intra-oceanic SDDS provides a viable physical mechanism for rapid plate-motion changes, such as those inferred for the African plate in the Late Cretaceous. Together, our results provide quantitative geodynamic support linking SDDS to major plate reorganizations.

Conflict of Interest

The authors declare no conflicts of interest relevant to this study.

Availability Statement

The parameter files to run all numerical models using ASPECT code are available in the following Zenodo repository (Guo et al., 2026).

Acknowledgments
We thank Ting Yang, an anonymous reviewer and the Associated Editor for helpful comments that significantly improved the manuscript. AFH was supported by the National Science Foundation (NSF; EAR-2147997) and computational resources were provided by NSF ACCESS (NSF; EAR-180026). We also thank the Computational Infrastructure for Geodynamics (geodynamics.org), which is funded by NSF EAR-0949446 and NSF EAR-1550901, for supporting the development of ASPECT.

References

Balázs, A., Faccenna, C., Ueda, K., Funiciello, F., Boutoux, A., Blanc, E. J.-P., & Gerya, T. (2021). Oblique subduction and mantle flow control on upper plate deformation: 3D geodynamic modeling. *Earth and Planetary Science Letters*, *569*, 117056. https://doi.org/10.1016/j.epsl.2021.117056

Bangerth, W., Dannberg, J., Fraters, M., Gassmoeller, R., Glerum, A., Heister, T., et al. (2023). ASPECT: Advanced solver for planetary evolution, convection, and tectonics, user manual. *Figshare*. https://doi.org/10.6084/m9.figshare.4865333

Behr, W. M., & Becker, T. W. (2018). Sediment control on subduction plate speeds. *Earth and Planetary Science Letters*, *502*, 166–173. https://doi.org/10.1016/j.epsl.2018.08.057

Bellahsen, N., Faccenna, C., & Funiciello, F. (2005). Dynamics of subduction and plate motion in laboratory experiments: Insights into the "plate tectonics" behavior of the Earth. *Journal of Geophysical Research*, *110*(B1), B01401. https://doi.org/10.1029/2004JB002999

Bercovici, D., Schubert, G., & Ricard, Y. (2015). Abrupt tectonics and rapid slab detachment with grain damage. *Proceedings of the National Academy of Sciences*, *112*(5), 1287–1291. https://doi.org/10.1073/pnas.1415473112

Besse, J., & Courtillot, V. (1988). Paleogeographic maps of the continents bordering the Indian Ocean since the Early Jurassic. *Journal of Geophysical Research*, *93*(B10), 11791–11808. https://doi.org/10.1029/JB093iB10p11791

Billen, M. I., & Hirth, G. (2007). Rheologic controls on slab dynamics. *Geochemistry, Geophysics, Geosystems*, *8*(8), Q08012. https://doi.org/10.1029/2007GC001597

Buffett, B. A. (2006). Plate force due to bending at subduction zones. *Journal of Geophysical Research*, *111*(B9), B09405. https://doi.org/10.1029/2006JB004295

Bull, J., DeMets, C., Krishna, K., Sanderson, D., & Merkouriev, S. (2010). Reconciling plate kinematic and seismic estimates of lithospheric convergence in the central Indian Ocean. *Geology*, *38*(4), 307–310. https://doi.org/10.1130/G30521.1

Cande, S., & Stegman, D. (2011). Indian and African plate motions driven by the push force of the Reunion plume head. *Nature*, *475*(7354), 47–52. https://doi.org/10.1038/nature10174

Chaillat, S., Gerardi, G., Li, Y., Chamolly, A., Li, Z.-H., & Ribe, N. M. (2024). The sphericity paradox and the role of hoop stresses in free subduction on a sphere. *Journal of Geophysical Research: Solid Earth*, *129*(9), e2024JB029500. https://doi.org/10.1029/2024JB029500

Chen, F., Davies, D. R., Goes, S., Suchoy, L., & Kramer, S. C. (2022). Comparing the dynamics of free subduction in Cartesian and spherical domains. *Geochemistry, Geophysics, Geosystems*, *23*(12), e2022GC010757. https://doi.org/10.1029/2022GC010757

Chen, F., Davies, D. R., Goes, S., Suchoy, L., & Kramer, S. C. (2024). The role of slab remnants in modulating free subduction dynamics: A 3-D spherical numerical study. *Geochemistry, Geophysics, Geosystems*, *25*(4), e2023GC011180. https://doi.org/10.1029/2023GC011180

Čížková, H., & Bina, C. R. (2013). Effects of mantle and subduction-interface rheologies on slab stagnation and trench rollback. *Earth and Planetary Science Letters*, *379*, 95–103. https://doi.org/10.1016/j.epsl.2013.08.011

Čížková, H., & Bina, C. R. (2015). Geodynamics of trench advance: Insights from a Philippine-Sea-style geometry. *Earth and Planetary Science Letters*, *430*, 408–415. https://doi.org/10.1016/j.epsl.2015.07.004

Clennett, E. J., Holt, A. F., Tetley, M. G., Becker, T. W., & Faccenna, C. (2023). Assessing plate reconstruction models using plate driving force consistency tests. *Scientific Reports*, *13*(1), 10191. https://doi.org/10.1038/s41598-023-37117-w

Coltice, N., Husson, L., Faccenna, C., & Arnould, M. (2019). What drives tectonic plates? *Science Advances*, *5*(10), eaax4295. https://doi.org/10.1126/sciadv.aax4295

Conrad, C. P., & Hager, B. H. (1999). Effects of plate bending and fault strength at subduction zones on plate dynamics. *Journal of Geophysical Research*, *104*(B8), 17551–17571. https://doi.org/10.1029/1999JB900149

Conrad, C. P., & Lithgow-Bertelloni, C. (2002). How mantle slabs drive plate tectonics. *Science*, *298*(5591), 207–209. https://doi.org/10.1126/science.1074161

Copley, A., Avouac, J.-P., & Royer, J.-Y. (2010). India-Asia collision and the Cenozoic slowdown of the Indian plate: Implications for the forces driving plate motions. *Journal of Geophysical Research*, *115*(B3), B03410. https://doi.org/10.1029/2009JB006634

Crameri, F., & Tackley, P. J. (2016). Subduction initiation from a stagnant lid and global overturn: New insights from numerical models with a free surface. *Progress in Earth and Planetary Science*, *3*(1), 30. https://doi.org/10.1186/s40645-016-0103-8

Cui, F., Li, Z.-H., & Fu, H.-Y. (2024). Quantitative evaluation of mantle flow traction on overlying tectonic plate: Linear versus power-law mantle rheology. *Geophysical Journal International*, *239*(2), 1063–1079. https://doi.org/10.1093/gji/ggae320

DeMets, C., Gordon, R. G., & Argus, D. F. (2010). Geologically current plate motions. *Geophysical Journal International*, *181*(1), 1–80. https://doi.org/10.1111/j.1365-246X.2009.04491.x

Di Leo, J. F., Walker, A. M., Li, Z.-H., Wookey, J., Ribe, N. M., Kendall, J.-M., & Tommasi, A. (2014). Development of texture and seismic anisotropy during the onset of subduction. *Geochemistry, Geophysics, Geosystems*, *15*(1), 192–212. https://doi.org/10.1002/2013GC005032

Domeier, M., Shephard, G. E., Jakob, J., Gaina, C., Doubrovine, P. V., & Torsvik, T. H. (2017). Intraoceanic subduction spanned the Pacific in the Late Cretaceous–Paleocene. *Science Advances*, *3*(11), eaao2303. https://doi.org/10.1126/sciadv.aao2303

Faccenna, C., Becker, T. W., Lallemand, S., & Steinberger, B. (2012). On the role of slab pull in the Cenozoic motion of the Pacific plate. *Geophysical Research Letters*, *39*(3), L03305. https://doi.org/10.1029/2011GL050155

Faccenna, C., Holt, A. F., Becker, T. W., Lallemand, S., & Royden, L. H. (2018). Dynamics of the Ryukyu/Izu-Bonin-Marianas double subduction system. *Tectonophysics*, *746*, 229–238. https://doi.org/10.1016/j.tecto.2017.08.011

Forsyth, D., & Uyeda, S. (1975). On the relative importance of the driving forces of plate motion. *Geophysical Journal International*, *43*(1), 163–200. https://doi.org/10.1111/j.1365-246X.1975.tb00631.x

Fraters, M. (2023). The geodynamic world builder [Dataset]. *Zenodo*. https://doi.org/10.5281/zenodo.7998525

Fraters, M., Bangerth, W., Thieulot, C., Glerum, A. C., & Spakman, W. (2019). Efficient and practical Newton solvers for non-linear Stokes systems in geodynamic problems. *Geophysical Journal International*, *218*(2), 873–894. https://doi.org/10.1093/gji/ggz183

Funiciello, F., Faccenna, C., Heuret, A., Lallemand, S., Di Giuseppe, E., & Becker, T. (2008). Trench migration, net rotation and slab–mantle coupling. *Earth and Planetary Science Letters*, *271*(1), 233–240. https://doi.org/10.1016/j.epsl.2008.04.006

Gerya, T. V., Stern, R. J., Baes, M., Sobolev, S. V., & Whattam, S. A. (2015). Plate tectonics on the Earth triggered by plume-induced subduction initiation. *Nature*, *527*(7577), 221–225. https://doi.org/10.1038/nature15752

Guo, Z., Holt, A., & Gürer, D. (2026). Model input files for "The impact of double subduction on plate velocity and Euler pole shifts: Insights From spherical subduction models" [Dataset]. *Zenodo*. https://doi.org/10.5281/zenodo.19056991

Gürer, D., Granot, R., & van Hinsbergen, D. J. J. (2022). Plate tectonic chain reaction revealed by noise in the Cretaceous quiet zone. *Nature Geoscience*, *15*(3), 233–239. https://doi.org/10.1038/s41561-022-00893-7

Gürer, D., van Hinsbergen, D. J. J., Matenco, L., Corfu, F., & Cascella, A. (2016). Kinematics of a former oceanic plate of the Neotethys revealed by deformation in the Ulukışla basin (Turkey). *Tectonics*, *35*(10), 2385–2416. https://doi.org/10.1002/2016TC004206

Hall, R. (2002). Cenozoic geological and plate tectonic evolution of SE Asia and the SW Pacific: Computer-based reconstructions, model and animations. *Journal of Asian Earth Sciences*, *20*(4), 353–431. https://doi.org/10.1016/S1367-9120(01)00069-4

Heister, T., Dannberg, J., Gassmöller, R., & Bangerth, W. (2017). High accuracy mantle convection simulation through modern numerical methods—II: Realistic models and problems. *Geophysical Journal International*, *210*(2), 833–851. https://doi.org/10.1093/gji/ggx195

Hirth, G., & Kohlstedt, D. (2003). Rheology of the upper mantle and the mantle wedge: A view from the experimentalists. *Geophysical Monograph Series*, *138*, 83–105. https://doi.org/10.1029/138GM06

Holt, A. F. (2022). The topographic signature of mantle pressure build-up beneath subducting plates: Insights from spherical subduction models. *Geophysical Research Letters*, *49*(22), e2022GL100330. https://doi.org/10.1029/2022GL100330

Holt, A. F., & Becker, T. W. (2016). The effect of a power-law mantle viscosity on trench retreat rate. *Geophysical Journal International*, *208*(1), 491–507. https://doi.org/10.1093/gji/ggw392

Holt, A. F., Royden, L., & Becker, T. (2017). The dynamics of double slab subduction. *Geophysical Journal International*, *209*(1), 250–265. https://doi.org/10.1093/gji/ggw496

Holt, A. F., Royden, L. H., Becker, T. W., & Faccenna, C. (2018). Slab interactions in 3-D subduction settings: The Philippine Sea plate region. *Earth and Planetary Science Letters*, *489*, 72–83. https://doi.org/10.1016/j.epsl.2018.02.024

Hu, J., Gurnis, M., Rudi, J., Stadler, G., & Müller, R. D. (2022). Dynamics of the abrupt change in Pacific Plate motion around 50 million years ago. *Nature Geoscience*, *15*(1), 74–78. https://doi.org/10.1038/s41561-021-00862-6

Iaffaldano, G., & Bunge, H.-P. (2015). Rapid plate motion variations through geological time: Observations serving geodynamic interpretation. *Annual Review of Earth and Planetary Sciences*, *43*(1), 571–592. https://doi.org/10.1146/annurev-earth-060614-105117

Iaffaldano, G., Bunge, H.-P., & Dixon, T. H. (2006). Feedback between mountain belt growth and plate convergence. *Geology*, *34*(10), 893–896. https://doi.org/10.1130/G22661.1

Jadamec, M. A., & Billen, M. I. (2010). Reconciling surface plate motions with rapid three-dimensional mantle flow around a slab edge. *Nature*, *465*(7296), 338–341. https://doi.org/10.1038/nature09053

Jagoutz, O., Royden, L., Holt, A. F., & Becker, T. W. (2015). Anomalously fast convergence of India and Eurasia caused by double subduction. *Nature Geoscience*, *8*(6), 475–478. https://doi.org/10.1038/ngeo2418

Jian, H., Yang, T., Chen, Z., Ye, L., Hu, J., & Guo, P. (2023). Slab pull drives IBM Trench advance despite the weakened Philippine Sea plate. *Geophysical Research Letters*, *50*(21), e2023GL106554. https://doi.org/10.1029/2023GL106554

Király, Á., Faccenna, C., & Funiciello, F. (2018). Subduction zones interaction around the Adria microplate and the origin of the Apenninic arc. *Tectonics*, *37*(10), 3941–3953. https://doi.org/10.1029/2018TC005211

Konstantinovskaia, E. (2001). Arc–continent collision and subduction reversal in the Cenozoic evolution of the Northwest Pacific: An example from Kamchatka (NE Russia). *Tectonophysics*, *333*(1), 75–94. https://doi.org/10.1016/S0040-1951(00)00268-7

Kreemer, C., Holt, W. E., & Haines, A. J. (2003). An integrated global model of present-day plate motions and plate boundary deformation. *Geophysical Journal International*, *154*(1), 8–34. https://doi.org/10.1046/j.1365-246X.2003.01917.x

Kronbichler, M., Heister, T., & Bangerth, W. (2012). High accuracy mantle convection simulation through modern numerical methods. *Geophysical Journal International*, *191*(1), 12–29. https://doi.org/10.1111/j.1365-246X.2012.05609.x

Lallemand, S., Font, Y., Bijwaard, H., & Kao, H. (2001). New insights on 3-D plates interaction near Taiwan from tomography and tectonic implications. *Tectonophysics*, *335*(3), 229–253. https://doi.org/10.1016/S0040-1951(01)00071-3

Lallemand, S., Heuret, A., Faccenna, C., & Funiciello, F. (2008). Subduction dynamics as revealed by trench migration. *Tectonics*, *27*(3), TC3014. https://doi.org/10.1029/2007TC002212

Lenardic, A., Weller, M., Höink, T., & Seales, J. (2019). Toward a boot strap hypothesis of plate tectonics: Feedbacks between plates, the asthenosphere, and the wavelength of mantle convection. *Physics of the Earth and Planetary Interiors*, *296*, 106299. https://doi.org/10.1016/j.pepi.2019.106299

Li, Y., Liu, L., Li, S., Peng, D., Cao, Z., & Li, X. (2024). Cenozoic India-Asia collision driven by mantle dragging the cratonic root. *Nature Communications*, *15*(1), 6674. https://doi.org/10.1038/s41467-024-51107-0

Lin, S.-C., & Kuo, B.-Y. (2016). Dynamics of the opposite-verging subduction zones in the Taiwan region: Insights from numerical models. *Journal of Geophysical Research: Solid Earth*, *121*(3), 2174–2192. https://doi.org/10.1002/2015JB012784

Lithgow-Bertelloni, C., & Richards, M. A. (1998). The dynamics of Cenozoic and Mesozoic plate motions. *Reviews of Geophysics*, *36*(1), 27–78. https://doi.org/10.1029/97RG02282

Liu, S., & King, S. D. (2022). Dynamics of the North American plate: Large-scale driving mechanism from far-field slabs and the interpretation of shallow negative seismic anomalies. *Geochemistry, Geophysics, Geosystems*, *23*(3), e2021GC009808. https://doi.org/10.1029/2021GC009808

Maffione, M., & van Hinsbergen, D. J. J. (2018). Reconstructing plate boundaries in the Jurassic neo-Tethys from the east and west Vardar ophiolites (Greece and Serbia). *Tectonics*, *37*(3), 858–887. https://doi.org/10.1002/2017TC004790

Mallard, C., Coltice, N., Seton, M., Müller, R. D., & Tackley, P. J. (2016). Subduction controls the distribution and fragmentation of Earth's tectonic plates. *Nature*, *535*(7610), 140–143. https://doi.org/10.1038/nature17992

Merkouriev, S., & DeMets, C. (2014). High-resolution Neogene reconstructions of Eurasia-North America Plate motion. *Geophysical Journal International*, *198*(1), 366–384. https://doi.org/10.1093/gji/ggu142

Mishin, Y. A., Gerya, T. V., Burg, J.-P., & Connolly, J. A. (2008). Dynamics of double subduction: Numerical modeling. *Physics of the Earth and Planetary Interiors*, *171*(1), 280–295. https://doi.org/10.1016/j.pepi.2008.06.012

Moresi, L., & Gurnis, M. (1996). Constraints on the lateral strength of slabs from three-dimensional dynamic flow models. *Earth and Planetary Science Letters*, *138*(1), 15–28. https://doi.org/10.1016/0012-821X(95)00221-W

Müller, R. D., Seton, M., Zahirovic, S., Williams, S. E., Matthews, K. J., Wright, N. M., et al. (2016). Ocean basin evolution and global-scale plate reorganization events since Pangea breakup. *Annual Review of Earth and Planetary Sciences*, *44*(1), 107–138. https://doi.org/10.1146/annurev-earth-060115-012211

Patočka, V., Čížková, H., & Pokorný, J. (2024). Dynamic component of the asthenosphere: Lateral viscosity variations due to dislocation creep at the base of oceanic plates. *Geophysical Research Letters*, *51*(13), e2024GL109116. https://doi.org/10.1029/2024GL109116

Patočka, V., Čížková, H., & Tackley, P. (2019). Do elasticity and a free surface affect lithospheric stresses caused by upper-mantle convection? *Geophysical Journal International*, *216*(3), 1740–1760. https://doi.org/10.1093/gji/ggy513

Pusok, A. E., & Stegman, D. R. (2019). Formation and stability of same-dip double subduction systems. *Journal of Geophysical Research: Solid Earth*, *124*(7), 7387–7412. https://doi.org/10.1029/2018JB017027

Pusok, A. E., & Stegman, D. R. (2020). The convergence history of India-Eurasia records multiple subduction dynamics processes. *Science Advances*, *6*(19), eaaz8681. https://doi.org/10.1126/sciadv.aaz8681

Ribe, N. M. (2010). Bending mechanics and mode selection in free subduction: A thin-sheet analysis. *Geophysical Journal International*, *180*(2), 559–576. https://doi.org/10.1111/j.1365-246X.2009.04460.x

Richards, M. A., & Lithgow-Bertelloni, C. (1996). Plate motion changes, the Hawaiian-Emperor Bend, and the apparent success and failure of geodynamic models. *Earth and Planetary Science Letters*, *137*(1), 19–27. https://doi.org/10.1016/0012-821X(95)00209-U

Richardson, R. M. (1992). Ridge forces, absolute plate motions, and the intraplate stress field. *Journal of Geophysical Research*, *97*(B8), 11739–11748. https://doi.org/10.1029/91JB00475

Schellart, W. P. (2009). Evolution of the slab bending radius and the bending dissipation in three-dimensional subduction models with a variable slab to upper mantle viscosity ratio. *Earth and Planetary Science Letters*, *288*(1), 309–319. https://doi.org/10.1016/j.epsl.2009.09.034

Schellart, W. P., Freeman, J., Stegman, D. R., Moresi, L., & May, D. (2007). Evolution and diversity of subduction zones controlled by slab width. *Nature*, *446*(7133), 308–311. https://doi.org/10.1038/nature05615

Seton, M., Müller, R., Zahirovic, S., Gaina, C., Torsvik, T., Shephard, G., et al. (2012). Global continental and ocean basin reconstructions since 200 Ma. *Earth-Science Reviews*, *113*(3), 212–270. https://doi.org/10.1016/j.earscirev.2012.03.002

Stampfli, G., & Borel, G. (2002). A plate tectonic model for the Paleozoic and Mesozoic constrained by dynamic plate boundaries and restored synthetic oceanic isochrons. *Earth and Planetary Science Letters*, *196*(1), 17–33. https://doi.org/10.1016/S0012-821X(01)00588-X

Stegman, D. R., Farrington, R., Capitanio, F. A., & Schellart, W. P. (2010). A regime diagram for subduction styles from 3-D numerical models of free subduction. *Tectonophysics*, *483*(1), 29–45. (Convergent plate margin dynamics: New perspectives from structural geology, geophysics and geodynamic modelling). https://doi.org/10.1016/j.tecto.2009.08.041

Stegman, D. R., Freeman, J., Schellart, W. P., Moresi, L., & May, D. (2006). Influence of trench width on subduction hinge retreat rates in 3-D models of slab rollback. *Geochemistry, Geophysics, Geosystems*, *7*(3), Q03012. https://doi.org/10.1029/2005GC001056

Stern, R. J. (2002). Subduction zones. *Reviews of Geophysics*, *40*(4), 3-1–3-38. https://doi.org/10.1029/2001RG000108

Tokle, L., Hufford, L. J., Behr, W. M., Morales, L. F. G., & Madonna, C. (2023). Diffusion creep of sodic amphibole-bearing blueschist limited by microboudinage. *Journal of Geophysical Research: Solid Earth*, *128*(9), e2023JB026848. https://doi.org/10.1029/2023JB026848

Torsvik, T. H., Van der Voo, R., Preeden, U., Mac Niocaill, C., Steinberger, B., Doubrovine, P. V., et al. (2012). Phanerozoic polar wander, palaeogeography and dynamics. *Earth-Science Reviews*, *114*(3), 325–368. https://doi.org/10.1016/j.earscirev.2012.06.007

Vaes, B., van Hinsbergen, D. J. J., & Boschman, L. M. (2019). Reconstruction of subduction and back-arc spreading in the NW Pacific and Aleutian Basin: Clues to causes of Cretaceous and Eocene plate reorganizations. *Tectonics*, *38*(4), 1367–1413. https://doi.org/10.1029/2018TC005164

van Benthem, S., Govers, R., Spakman, W., & Wortel, R. (2013). Tectonic evolution and mantle structure of the Caribbean. *Journal of Geophysical Research: Solid Earth*, *118*(6), 3019–3036. https://doi.org/10.1002/jgrb.50235

van der Wiel, E., Pokorný, J., Čížková, H., Spakman, W., van den Berg, A. P., & van Hinsbergen, D. J. J. (2024). Slab buckling as a driver for rapid oscillations in Indian plate motion and subduction rate. *Communications Earth & Environment*, *5*(1), 316. https://doi.org/10.1038/s43247-024-01472-x

van Hinsbergen, D. J. J., Steinberger, B., Guilmette, C., Maffione, M., Gürer, D., Peters, K., et al. (2021). A record of plume-induced plate rotation triggering subduction initiation. *Nature Geoscience*, *14*(8), 626–630. https://doi.org/10.1038/s41561-021-00780-7

van Hinsbergen, D. J. J., Torsvik, T. H., Schmid, S. M., Matenco, L. C., Maffione, M., Vissers, R. L., et al. (2020). Orogenic architecture of the Mediterranean region and kinematic reconstruction of its tectonic evolution since the Triassic. *Gondwana Research*, *81*, 79–229. https://doi.org/10.1016/j.gr.2019.07.009

Vignaroli, G., Faccenna, C., Jolivet, L., Piromallo, C., & Rossetti, F. (2008). Subduction polarity reversal at the junction between the Western Alps and the Northern Apennines, Italy. *Tectonophysics*, *450*(1), 34–50. https://doi.org/10.1016/j.tecto.2007.12.012

Wada, I., He, J., Hasegawa, A., & Nakajima, J. (2015). Mantle wedge flow pattern and thermal structure in Northeast Japan: Effects of oblique subduction and 3-D slab geometry. *Earth and Planetary Science Letters*, *426*, 76–88. https://doi.org/10.1016/j.epsl.2015.06.021

Wang, C., Ding, W., Schellart, W. P., Tong, Z., Dong, C., Fang, Y., & Li, J. (2024). Effects of along-trench asymmetric subduction initiation on plate rotation and trench migration: A laboratory modeling perspective. *Tectonics*, *43*(1), e2023TC007941. https://doi.org/10.1029/2023TC007941

Wu, J., Wu, T.-J., & Yamaoka, K. (2024). Linking Pacific plate motions to metamorphism and magmatism in Japan during Cretaceous to Paleogene times. *Elements*, *20*(2), 103–109. https://doi.org/10.2138/gselements.20.2.103

Xue, K., Schellart, W. P., & Strak, V. (2020). Effect of plate length on subduction kinematics and slab geometry: Insights from buoyancy-driven analog subduction models. *Journal of Geophysical Research: Solid Earth*, *125*(11), e2020JB020514. https://doi.org/10.1029/2020JB020514

Yamato, P., Husson, L., Braun, J., Loiselet, C., & Thieulot, C. (2009). Influence of surrounding plates on 3D subduction dynamics. *Geophysical Research Letters*, *36*(7),L07303. https://doi.org/10.1029/2008GL036942

Zhang, J., & Hu, J. (2025). Dynamics of longitudinal Hawaiian hotspot motion and the formation of the Hawaiian-Emperor Bend. *Proceedings of the National Academy of Sciences*, *122*(39), e2510972122. https://doi.org/10.1073/pnas.2510972122

Zhang, K., Liao, J., & Gerya, T. (2024). Onset of double subduction controls plate motion reorganisation. *Nature Communications*, *15*(1), 1513. https://doi.org/10.1038/s41467-024-44764-8

Zhang, Q., Guo, F., Zhao, L., & Wu, Y. (2017). Geodynamics of divergent double subduction: 3-D numerical modeling of a Cenozoic example in the Molucca Sea region, Indonesia. *Journal of Geophysical Research: Solid Earth*, *122*(5), 3977–3998. https://doi.org/10.1002/2017JB013991

Zhong, S., Gurnis, M., & Moresi, L. (1998). Role of faults, nonlinear rheology, and viscosity structure in generating plates from instantaneous mantle flow models. *Journal of Geophysical Research*, *103*(B7), 15255–15268. https://doi.org/10.1029/98JB00605